

International Journal of Modern Physics E
© World Scientific Publishing Company

THE MICROSCOPIC APPROACH TO NUCLEAR MATTER AND NEUTRON STAR MATTER

FRANCESCA SAMMARRUCA

*Physics Department, University of Idaho
Moscow, Idaho 83844, U.S.A.
fsammarr@uidaho.edu*

Received (received date)

Revised (revised date)

We review a variety of theoretical and experimental investigations aimed at improving our knowledge of the nuclear matter equation of state. Of particular interest are nuclear matter extreme states in terms of density and/or isospin asymmetry. The equation of state of matter with unequal concentrations of protons and neutrons has numerous applications. These include heavy-ion collisions, the physics of rare, short-lived nuclei and, on a dramatically different scale, the physics of neutron stars. The “common denominator” among these (seemingly) very different systems is the symmetry energy, which plays a crucial role in both the formation of the neutron skin in neutron-rich nuclei and the radius of a neutron star (a system 18 orders of magnitude larger and 55 orders of magnitudes heavier). The details of the density dependence of the symmetry energy are not yet sufficiently constrained. Throughout this article, our emphasis will be on the importance of adopting a microscopic approach to the many-body problem, which we believe to be the one with true predictive power.

1. Introduction

The interaction of hadrons in nuclei is a problem that goes to the very core of nuclear physics. In fact, our present knowledge of the nuclear force in free space is, in itself, the result of decades of struggle,¹ which will not be reviewed in this article. The nature of the nuclear force in the medium is of course a much more complex problem, as it involves aspects of the force that cannot be constrained through free-space nucleon-nucleon (NN) scattering. Predictions of properties of nuclei are the ultimate test for many-body theories.

Nuclear matter is an alternative and convenient theoretical laboratory for many-body theories. By “nuclear matter” we mean an infinite system of nucleons acted on by their mutual strong forces and no electromagnetic interactions. Nuclear matter is characterized by its energy/particle as a function of density and other thermodynamic quantities, if appropriate (e.g. temperature). Such relation is known as the nuclear matter equation of state (EoS). The translational invariance of the system facilitates theoretical calculations. At the same time, adopting what is known as “local density approximation”, one can use the EoS directly in calculations of finite systems. This procedure is applied, for instance, in Thomas-Fermi calculations within the liquid drop model, where an appropriate energy functional is written in terms of the EoS.^{2,3,4}

Symmetric nuclear matter (that is, matter with equal densities of protons and neutrons) has been studied extensively. The so-called conventional approach goes back to earlier works by Brueckner and others^{5,6,7,8} and is known as the Brueckner-Hartree-Fock (BHF) theory. The Brueckner theory is based on a linked-cluster perturbation series of the ground state energy of a many-body system.^{5,6,7,8,9,10} Such series was shown to converge when the cluster diagrams are regrouped according to the number of hole lines. The variational approach was also pursued as an alternative method^{11,12} and yielded predictions in close agreement with those from Brueckner theory when realistic NN potentials were employed.¹³

During the 1980’s, the Dirac-Brueckner-Hartree-Fock (DBHF) approach was developed.^{14,15,16} The main break-through came with the observation that the DBHF theory, unlike conventional Brueckner theory, could describe successfully the saturation properties of nuclear matter, that is, saturation energy and density of the equation of state. The DBHF method adopts realistic NN interactions and contains important relativistic features. It describes the nuclear mean field in terms of strong, competing scalar and vector fields that, together, account for the binding of nucleons as well as the large spin-orbit splitting seen in nuclear states.

Regardless of the chosen many-body theory, a quantitative NN potential should be part of its input. Recently, chiral effective theories of the nuclear force¹⁷ have become popular as a mean to respect the symmetries of Quantum Chromo Dynamics (QCD) while retaining the basic degrees of freedom typical of low-energy nuclear physics. Chiral effective theories provide a well-defined scheme to determine the appropriate many-body diagrams to be included at each order of the perturbation.

However, being based on a low-momentum expansion, interactions derived from chiral perturbation theory are not suitable for applications in dense nuclear/neutron matter, where high Fermi momenta are involved. Instead, meson-theoretic or phenomenological NN potentials are typically employed as input to the many-body theory. Mean-field models (relativistic and non-relativistic) are a popular, although non-microscopic, alternative to methods based on the in-medium reaction matrix, such as BHF and DBHF.

It is the purpose of this article to review the status of microscopic studies of nuclear and neutron-rich matter, with particular emphasis on the latter, as it relates to present empirical investigations within terrestrial laboratories (heavy-ion collisions) or astrophysical observations (neutron stars). At the same time, we will review the present status concerning available empirical information which can be utilized to guide and constrain theories. We also wish to provide a self-contained account of the recent work with asymmetric matter done by the Idaho group, including extensive numerical tables for the interested user.

Clearly, the goal to describe the properties of (dense) many-body systems consistently from the underlying forces *and* including all potentially important mechanisms, is a most ambitious program and far from having been completed. The importance of pursuing a microscopic approach towards the accomplishment of this goal is a theme that will surface repeatedly throughout this article.

2. Asymmetric Nuclear Matter: Some Facts and Phenomenology

Isospin-asymmetric nuclear matter (IANM) simulates the interior of a “nucleus” with unequal densities of protons and neutrons. The equation of state of (cold) IANM is then a function of density as well as the relative concentrations of protons and neutrons.

The recent and fast-growing interest in IANM stems from its close connection to neutron-rich nuclei, or, more generally, asymmetric nuclei, including the very “exotic” ones known as “halo” nuclei. At this time, the boundaries of the nuclear chart are uncertain, with a few hundreds stable nuclides known to exist and perhaps a few thousands believed to exist. The Facility for Rare Isotope Beams (FRIB) has recently been approved for design and construction at Michigan State University (MSU). The facility will deliver intense beams of rare isotopes, the study of which can provide crucial information on short-lived elements normally not found on earth.¹⁸ Thus, this new experimental program will have widespread impact, ranging from the origin of elements to the evolution of the cosmos.

It is estimated that the design and construction of FRIB will take ten years.¹⁸ In the meantime, systematic investigations to determine the properties of asymmetric nuclear matter are proliferating at existing facilities.

From the theoretical side, some older studies of IANM can be found in Refs.^{19,20} Interactions adjusted to fit properties of finite nuclei, such as those based on the non-relativistic Skyrme Hartree-Fock theory²¹ or the relativistic mean field theory,²²

have been used to extract phenomenological EoS. Variational calculations of asymmetric matter have also been reported.^{12,23} Fuchs *et al.*²⁴ defined a Lorentz invariant functional of the baryon field operators to project Dirac-Brueckner nuclear matter results onto the meson-nucleon vertices of an effective density-dependent field theory. This was then applied to asymmetric matter and finite nuclei in Hartree calculations.²⁵ Extensive work with IANM has also been reported by Lombardo and collaborators.^{26,27} Dirac-Brueckner-Hartree-Fock calculations of IANM properties were performed by the Oslo group,²⁸ the Idaho group,²⁹ and by Fuchs and collaborators.³⁰ Typically, considerable model dependence is observed among the different EoS of IANM, especially in the high-density region.

Asymmetric nuclear matter can be characterized by the neutron density, ρ_n , and the proton density, ρ_p , defined as the number of neutrons or protons per unit of volume. In infinite matter, they are obtained by summing the neutron or proton states per volume (up to their respective Fermi momenta, k_F^n or k_F^p) and applying the appropriate degeneracy factor. The result is

$$\rho_i = \frac{(k_F^i)^3}{3\pi^2}, \quad (1)$$

with $i = n$ or p .

It is more convenient to refer to the total density $\rho = \rho_n + \rho_p$ and the asymmetry (or neutron excess) parameter $\alpha = \frac{\rho_n - \rho_p}{\rho}$. Clearly, $\alpha=0$ corresponds to symmetric matter and $\alpha=1$ to neutron matter. In terms of α and the average Fermi momentum, k_F , related to the total density in the usual way,

$$\rho = \frac{2k_F^3}{3\pi^2}, \quad (2)$$

the neutron and proton Fermi momenta can be expressed as

$$k_F^n = k_F(1 + \alpha)^{1/3} \quad (3)$$

and

$$k_F^p = k_F(1 - \alpha)^{1/3}, \quad (4)$$

respectively.

The energy/particle in IANM can, to a very good degree of approximation, be written as

$$e(\rho, \alpha) \approx e_0(\rho) + e_{sym}(\rho)\alpha^2, \quad (5)$$

where the first term is the energy/particle in symmetric matter and e_{sym} is known as the symmetry energy. In the Bethe-Weizsäcker formula for the nuclear binding energy, it represents the amount of binding a nucleus has to lose when the numbers of protons and neutrons are unequal. The symmetry energy is also closely related to the neutron β -decay in dense matter, whose threshold depends on the proton fraction. A typical value for e_{sym} at nuclear matter density (ρ_0) is 30 MeV, with theoretical predictions spreading approximately between 26 and 35 MeV. The effect

of a term of fourth order in the asymmetry parameter ($\mathcal{O}(\alpha^4)$) on the bulk properties of neutron stars is very small, although it may impact the proton fraction at high density. More generally, non-quadratic terms are usually associated with isovector pairing, which is a surface effect and thus vanishes in infinite matter.³¹

Equation (5) displays a convenient separation between the symmetric and asymmetric parts of the EoS, which facilitates the identification of observables that may be sensitive, for instance, mainly to the symmetry energy. At this time, groups from GSI,³² MSU,³³ Italy,³⁴ France,³⁵ and China^{36,37,38} are investigating the density dependence of the symmetry energy through heavy-ion collisions. From recent results, such as those reported at the 2009 “International Workshop on Nuclear Dynamics in Heavy-ion Reactions and the Symmetry Energy” (Shanghai, China, August 22-25, 2009), these investigations appear to agree reasonably well on the following parametrization of the symmetry energy:

$$e_{sym}(\rho) = 12.5 \text{ MeV} \left(\frac{\rho}{\rho_0} \right)^{2/3} + 17.5 \text{ MeV} \left(\frac{\rho}{\rho_0} \right)^{\gamma_i}, \quad (6)$$

where the first term is the kinetic contribution and γ_i (the exponent appearing in the potential energy part) is found to be between 0.4 and 1.0. Naturally, there are uncertainties associated with all transport models. Recent constraints from MSU³³ were extracted from simulations of ^{112}Sn and ^{124}Sn collisions with an Improved Quantum Molecular Dynamics transport model and are consistent with isospin diffusion data and the ratio of neutron and proton spectra.

Typically, parametrizations like the one given in Eq. (6) are valid at or below the saturation density, ρ_0 . Efforts to constrain the behavior of the symmetry energy at higher densities are presently being pursued through observables such as π^-/π^+ ratio, K^+/K^0 ratio, neutron/proton differential transverse flow, or nucleon elliptic flow.³⁹

A more detailed discussion of the symmetry energy and the status of its theoretical predictions will be presented in Sec. 3.2.3.

3. The Microscopic Approach

In this section, we present a discussion of the microscopic approach to nuclear matter, in general, and the DBHF method, in particular.

3.1. The two-body potential

By *ab initio* we mean that the starting point of the many-body calculation is a realistic NN interaction which is then applied in the nuclear medium without any additional free parameters. Thus the first question to be confronted concerns the choice of the “best” NN interaction. As already mentioned in the Introduction, after the development of QCD and the understanding of its symmetries, chiral effective theories¹⁷ were developed as a way to respect the symmetries of QCD while keeping the degrees of freedom (nucleons and pions) typical of low-energy nuclear physics.

However, chiral perturbation theory (ChPT) has definite limitations as far as the range of allowed momenta is concerned. For the purpose of applications in dense matter, where higher and higher momenta become involved with increasing Fermi momentum, NN potentials based on ChPT are unsuitable.

Relativistic meson theory is an appropriate framework to deal with the high momenta encountered in dense matter. In particular, the one-boson-exchange (OBE) model has proven very successful in describing NN data in free space and has a good theoretical foundation. Among the many available OBE potentials, some being part of the “high-precision generation”,^{40,41,42} we seek a momentum-space potential developed within a relativistic scattering equation, such as the one obtained through the Thompson⁴³ three-dimensional reduction of the Bethe-Salpeter equation.⁴⁴ Furthermore, we require a potential that uses the pseudovector coupling for the interaction of nucleons with pseudoscalar mesons. With these constraints in mind, as well as the requirement of a good description of the NN data, Bonn B¹ is a reasonable choice. As is well known, the NN potential model dependence of nuclear matter predictions is not negligible. The saturation points obtained with different NN potentials move along the famous “Coester band” depending on the strength of the tensor force, with the weakest tensor force yielding the largest attraction. This can be understood in terms of medium effects (particularly Pauli blocking) reducing the (attractive) second-order term in the expansion of the reaction matrix. A large second-order term will undergo a large reduction in the medium. Therefore, noticing that the second-order term is dominated by the tensor component of the force, nuclear potentials with a strong tensor component will yield less attraction in the medium. For the same reason (that is, the role of the tensor force in nuclear matter), the potential model dependence is strongly reduced in pure (or nearly pure) neutron matter, due to the absence of isospin-zero partial waves.

Already when QCD (and its symmetries) were unknown, it was observed that the contribution from the nucleon-antinucleon pair diagram, Fig. 1, becomes unreasonably large if the pseudoscalar (ps) coupling is used, leading to very large pion-nucleon scattering lengths.⁴⁵ We recall that the Lagrangian density for pseudoscalar coupling of the nucleon field (ψ) with the pseudoscalar meson field (ϕ) is

$$\mathcal{L}_{ps} = -ig_{ps}\bar{\psi}\gamma_5\psi\phi. \quad (7)$$

On the other hand, the same contribution (Fig. 1) is heavily reduced by the pseudovector (pv) coupling (a mechanism which became known as “pair suppression”). The reason for the suppression is the presence of the covariant derivative at the pseudovector vertex,

$$\mathcal{L}_{pv} = \frac{f_{ps}}{m_{ps}}\bar{\psi}\gamma_5\gamma^\mu\psi\partial_\mu\phi, \quad (8)$$

which reduces the contribution of the vertex for low momenta and, thus, explains the small value of the pion-nucleon scattering length at threshold.⁴⁵ Considerations

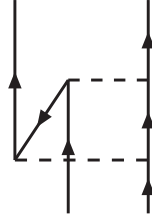


Fig. 1. Contribution to the NN interaction from virtual pair excitation. Upward- and downward-pointing arrows represent nucleons and antinucleons, respectively. Dashed lines denote mesons.

based on chiral symmetry⁴⁵ can further motivate the choice of the pseudovector coupling.

In closing this section, we wish to highlight the most important aspect of the “*ab initio*” approach: namely, the only free parameters of the model (the parameters of the NN potential) are determined by fitting the free-space NN data and never readjusted in the medium. In other words, the model parameters are tightly constrained and the calculation in the medium is parameter free. The presence of free parameters in the medium would generate effects and sensitivities which are hard to control and interfere with the predictive power of the theory.

3.2. The Dirac-Brueckner-Hartree-Fock approach to symmetric and asymmetric nuclear matter

3.2.1. Formalism

The main strength of the DBHF approach is in its inherent ability to account for important three-body forces through its density dependence. In Fig. 2 we show a three-body force (TBF) originating from virtual excitation of a nucleon-antinucleon pair, known as “Z-diagram”. Notice that the observations from the previous section ensure that the corresponding diagram at the two-body level, Fig. 1, is moderate in size when the pv coupling is used. The main feature of the DBHF method turns out to be closely related to the TBF depicted in Fig. 2, as we will argue next. In the DBHF approach, one describes the positive energy solutions of the Dirac equation in the medium as

$$u^*(p, \lambda) = \left(\frac{E_p^* + m^*}{2m^*} \right)^{1/2} \begin{pmatrix} \mathbf{1} \\ \frac{\boldsymbol{\sigma} \cdot \vec{p}}{E_p^* + m^*} \end{pmatrix} \chi_\lambda, \quad (9)$$

where the effective mass, m^* , is defined as $m^* = m + U_S$, with U_S an attractive scalar potential. (This will be derived below.) It can be shown that both the description of a single-nucleon via Eq. (9) and the evaluation of the Z-diagram, Fig. 2, generate a

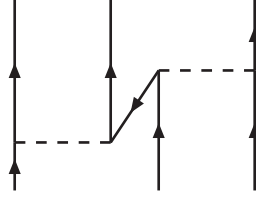


Fig. 2. Three-body force due to virtual pair excitation. Conventions as in the previous figure.

repulsive effect on the energy/particle in symmetric nuclear matter which depends on the density approximately as

$$\Delta E \propto \left(\frac{\rho}{\rho_0} \right)^{8/3}, \quad (10)$$

and provides the saturating mechanism missing from conventional Brueckner calculations. (Alternatively, explicit TBF are used along with the BHF method in order to achieve a similar result.) Brown showed that the bulk of the desired effect can be obtained as a lowest order (in p^2/m) relativistic correction to the single-particle propagation.⁴⁶ With the in-medium spinor as in Eq. (9), the correction to the free-space spinor can be written approximately as

$$u^*(p, \lambda) - u(p, \lambda) \approx \begin{pmatrix} \mathbf{0} \\ -\frac{\sigma \cdot \vec{p}}{2m^2} U_S \end{pmatrix} \chi_\lambda, \quad (11)$$

where for simplicity the spinor normalization factor has been set equal to 1, in which case it is clearly seen that the entire effect originates from the modification of the spinor's lower component. By expanding the single-particle energy to order U_S^2 , Brown showed that the correction to the energy consistent with Eq. (11) can be written as $\frac{p^2}{2m} (\frac{U_S}{m})^2$. He then proceeded to estimate the correction to the energy/particle and found it to be approximately as given in Eq. (10).

The approximate equivalence of the effective-mass description of Dirac states and the contribution from the Z-diagram has a simple intuitive explanation in the observation that Eq. (9), like any other solution of the Dirac equation, can be written as a superposition of positive and negative energy solutions. On the other hand, the “nucleon” in the middle of the Z-diagram, Fig. 2, is precisely a superposition of positive and negative energy states. In summary, the DBHF method effectively takes into account a particular class of TBF, which are crucial for nuclear matter saturation.

Of course, other, more popular, three-body forces (not included in DBHF) need to be addressed as well. Figure 3 shows the TBF that is included in essentially all TBF models, regardless other components; it is the Fujita-Miyazawa TBF.⁴⁷ With the addition of contributions from πN S-waves, one ends up with the well-known

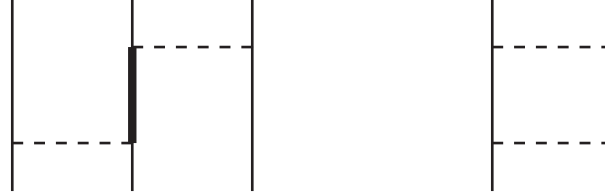


Fig. 3. Left: three-body force arising from Δ -isobar excitation (thick line). Right: two-meson exchange contribution to the NN interaction involving Δ -isobar excitation.

Tucson-Melbourne TBF.⁴⁸ The microscopic TBF of Ref.⁴⁹ includes contributions from excitation of the Roper resonance (P_{11} isobar) as well.

Now, if diagrams such as the one shown on the left-hand side of Fig. 3 are taken into account, consistency requires that medium modifications at the corresponding two-body level are also included, that is, the diagram on the right-hand side of Fig. 3 should be present and properly medium modified. Large cancellations then take place, a fact that was brought up a long time ago.⁵⁰ When the two-body sector is handled via OBE diagrams, the two-pion exchange is effectively incorporated through the σ “meson”, which cannot generate the (large) medium effects (dispersion and Pauli blocking on Δ intermediate states) required by the consistency arguments presented above. Thus, caution needs to be exercised when applying TBF in a particular space (of nucleons only, or nucleons and Δ).

Having first summarized the main DBHF philosophy, we now proceed to describe the DBHF calculation of IANM.²⁹ In the end, this will take us back to the crucial point of the DBHF approximation, Eq. (9).

We start from the Thompson⁴³ relativistic three-dimensional reduction of the Bethe-Salpeter equation.⁴⁴ The Thompson equation is applied to nuclear matter in strict analogy to free-space scattering and reads, in the nuclear matter rest frame,

$$g_{ij}(\vec{q}', \vec{q}, \vec{P}, (\epsilon_{ij}^*)_0) = v_{ij}^*(\vec{q}', \vec{q}) + \int \frac{d^3K}{(2\pi)^3} v_{ij}^*(\vec{q}', \vec{K}) \frac{m_i^* m_j^*}{E_i^* E_j^*} \frac{Q_{ij}(\vec{K}, \vec{P})}{(\epsilon_{ij}^*)_0 - \epsilon_{ij}^*(\vec{P}, \vec{K})} g_{ij}(\vec{K}, \vec{q}, \vec{P}, (\epsilon_{ij}^*)_0), \quad (12)$$

where g_{ij} is the in-medium reaction matrix ($ij=nn$, pp , or np), and the asterisk signifies that medium effects are applied to those quantities. Thus the NN potential, v_{ij}^* , is constructed in terms of effective Dirac states (in-medium spinors) as explained above. In Eq. (12), \vec{q} , \vec{q}' , and \vec{K} are the initial, final, and intermediate relative momenta, and $E_i^* = \sqrt{(m_i^*)^2 + K^2}$. The momenta of the two interacting particles in the nuclear matter rest frame have been expressed in terms of their relative

momentum and the center-of-mass momentum, \vec{P} , through

$$\vec{P} = \vec{k}_1 + \vec{k}_2, \quad (13)$$

$$\vec{K} = \frac{\vec{k}_1 - \vec{k}_2}{2}. \quad (14)$$

The energy of the two-particle system is

$$\epsilon_{ij}^*(\vec{P}, \vec{K}) = e_i^*(\vec{P}, \vec{K}) + e_j^*(\vec{P}, \vec{K}) \quad (15)$$

and $(\epsilon_{ij}^*)_0$ is the starting energy. The single-particle energy e_i^* includes kinetic energy and potential energy contributions (see Eq. (29) below). The Pauli operator, Q_{ij} , prevents scattering to occupied nn , pp , or np states. To eliminate the angular dependence from the kernel of Eq. (12), it is customary to replace the exact Pauli operator with its angle-average. Detailed expressions for the Pauli operator and the average center-of-mass momentum in the case of two different Fermi seas can be found in Ref.²⁹.

With the definitions

$$G_{ij} = \frac{m_i^*}{E_i^*(\vec{q}')} g_{ij} \frac{m_j^*}{E_j^*(\vec{q})} \quad (16)$$

and

$$V_{ij}^* = \frac{m_i^*}{E_i^*(\vec{q}')} v_{ij}^* \frac{m_j^*}{E_j^*(\vec{q})}, \quad (17)$$

one can rewrite Eq. (12) as

$$\begin{aligned} G_{ij}(\vec{q}', \vec{q}, \vec{P}, (\epsilon_{ij}^*)_0) &= V_{ij}^*(\vec{q}', \vec{q}) \\ &+ \int \frac{d^3K}{(2\pi)^3} V_{ij}^*(\vec{q}', \vec{K}) \frac{Q_{ij}(\vec{K}, \vec{P})}{(\epsilon_{ij}^*)_0 - \epsilon_{ij}^*(\vec{P}, \vec{K})} G_{ij}(\vec{K}, \vec{q}, \vec{P}, (\epsilon_{ij}^*)_0), \end{aligned} \quad (18)$$

which is formally identical to its non-relativistic counterpart.

The goal is to determine self-consistently the nuclear matter single-particle potential which, for IANM, will be different for neutrons and protons. To facilitate the description of the procedure, we will use a schematic notation for the neutron/proton potential. We write, for neutrons,

$$U_n = U_{np} + U_{nn}, \quad (19)$$

and for protons

$$U_p = U_{pn} + U_{pp}, \quad (20)$$

where each of the four pieces on the right-hand-side of Eqs. (19-20) signifies an integral of the appropriate G -matrix (nn , pp , or np) obtained from Eq. (18). Clearly, the two equations above are coupled through the np component and so they must be solved simultaneously. Furthermore, the G -matrix equation and Eqs. (19-20)

are coupled through the single-particle energy (which includes the single-particle potential, itself defined in terms of the G -matrix). So we have a coupled system to be solved self-consistently.

Before proceeding with the self-consistency, one needs an *ansatz* for the single-particle potential. The latter is suggested by the most general structure of the nucleon self-energy operator consistent with all symmetry requirements. That is:

$$\mathcal{U}_i(\vec{p}) = U_{S,i}(p) + \gamma_0 U_{V,i}^0(p) - \gamma \cdot \vec{p} U_{V,i}(p), \quad (21)$$

where $U_{S,i}$ and $U_{V,i}$ are an attractive scalar field and a repulsive vector field, respectively, with $U_{V,i}^0$ the timelike component of the vector field. These fields are in general density and momentum dependent. We take

$$\mathcal{U}_i(\vec{p}) \approx U_{S,i}(p) + \gamma_0 U_{V,i}^0(p), \quad (22)$$

which amounts to assuming that the spacelike component of the vector field is much smaller than both $U_{S,i}$ and $U_{V,i}^0$. Furthermore, neglecting the momentum dependence of the scalar and vector fields and inserting Eq. (22) in the Dirac equation for neutrons/protons propagating in nuclear matter,

$$(\gamma_\mu p^\mu - m_i - \mathcal{U}_i(\vec{p}))u_i(\vec{p}, \lambda) = 0, \quad (23)$$

naturally leads to rewriting the Dirac equation in the form

$$(\gamma_\mu p^{\mu*} - m_i^*)u_i(\vec{p}, \lambda) = 0, \quad (24)$$

with positive energy solutions as in Eq. (9), $m_i^* = m + U_{S,i}$, and

$$(p^0)^* = p^0 - U_{V,i}^0(p). \quad (25)$$

The subscript “ i ” signifies that these parameters are different for protons and neutrons.

As in the symmetric matter case,¹⁶ evaluating the expectation value of Eq. (22) leads to a parametrization of the single particle potential for protons and neutrons (Eqs.(19-20)) in terms of the constants $U_{S,i}$ and $U_{V,i}^0$ which is given by

$$U_i(p) = \frac{m_i^*}{E_i^*} \langle \vec{p} | \mathcal{U}_i(\vec{p}) | \mathbf{p} \rangle = \frac{m_i^*}{E_i^*} U_{S,i} + U_{V,i}^0. \quad (26)$$

Also,

$$U_i(p) = \sum_{p_j' \leq k_F^i} G_{ij}(\vec{p}_i, \vec{p}_j'), \quad (27)$$

which, along with Eq. (26), allows the self-consistent determination of the single-particle potential as explained below.

The kinetic contribution to the single-particle energy is

$$T_i(p) = \frac{m_i^*}{E_i^*} \langle \vec{p} | \gamma \cdot \vec{p} + m | \vec{p} \rangle = \frac{m_i m_i^* + \vec{p}^2}{E_i^*}, \quad (28)$$

and the single-particle energy is

$$e_i^*(p) = T_i(p) + U_i(p) = E_i^* + U_{V,i}^0. \quad (29)$$

The constants m_i^* and

$$U_{0,i} = U_{S,i} + U_{V,i}^0 \quad (30)$$

are convenient to work with as they facilitate the connection with the usual non-relativistic framework.⁹

Starting from some initial values of m_i^* and $U_{0,i}$, the G -matrix equation is solved and a first approximation for $U_i(p)$ is obtained by integrating the G -matrix over the appropriate Fermi sea, see Eq. (27). This solution is again parametrized in terms of a new set of constants, determined by fitting the parametrized U_i , Eq. (26), to its values calculated at two momenta, a procedure known as the “reference spectrum approximation”. The iterative procedure is repeated until convergence is reached.

Finally, the energy per neutron or proton in nuclear matter is calculated from

$$\bar{e}_i = \frac{1}{A} \langle T_i \rangle + \frac{1}{2A} \langle U_i \rangle - m. \quad (31)$$

The EoS, or energy per nucleon as a function of density, is then written as

$$\bar{e}(\rho_n, \rho_p) = \frac{\rho_n \bar{e}_n + \rho_p \bar{e}_p}{\rho}, \quad (32)$$

or

$$\bar{e}(k_F, \alpha) = \frac{(1 + \alpha)\bar{e}_n + (1 - \alpha)\bar{e}_p}{2}. \quad (33)$$

Clearly, symmetric nuclear matter is obtained as a by-product of the calculation described above by setting $\alpha=0$.

In the DBHF calculation of Ref.³⁰, a similar scheme is applied to obtain the self-consistent G -matrix and spinor basis. At each step of the iterative procedure, the nucleon self-energy is first calculated by integrating the G -matrix elements over the Fermi sea. The self-energy components are then obtained from the appropriate traces³⁰, i. e.

$$\Sigma_S = \frac{1}{4} \text{tr}[\Sigma], \quad \Sigma_0 = -\frac{1}{4} \text{tr}[\gamma_0 \Sigma], \quad \Sigma_V = -\frac{1}{4|\vec{p}|^2} \text{tr}[\gamma \cdot \vec{p} \Sigma]. \quad (34)$$

A covariant representation of the G -matrix is used to facilitate the transitions between the two-nucleon center-of-mass frame and the nuclear matter rest frame. Again, the presence of the medium naturally leads to define an effective mass, which is given by³⁰

$$m^*(p, k_F) = (m + \text{Re}\Sigma_S(p, k_F)) / (1 + \Sigma_V(p, k_F)). \quad (35)$$

Although the effective mass is density and momentum dependent, ultimately it is defined as the value of the expression given in Eq. (35) at $p = k_F$. Thus, the “reference spectrum approximation” is also employed in Ref.³⁰, although differently in some of the technical aspects as compared to the Idaho method. These technical aspects appear to impact the predictions of some isovector quantities, as it will be discussed in Sec. 3.2.4.

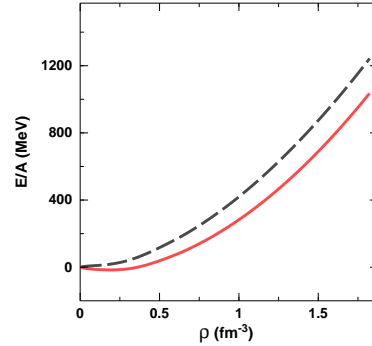


Fig. 4. DBHF predictions for the EoS of symmetric matter (solid red) and neutron matter (dashed black).

3.2.2. EoS predictions with the DBHF approach

In Fig. 4, we show EoS predictions for symmetric matter (solid red) and neutron matter (dashed black) as obtained from the Idaho calculation described in the previous section. Equation (4) then gives the EoS values for any α , a behavior which can be verified to be approximately true.²⁹

The EoS from DBHF can be characterized as being moderately soft at low to medium density and fairly “stiff” at high densities. The predicted saturation density and energy for the symmetric matter EoS in Fig. 4 are equal to 0.185 fm^{-3} and -16.14 MeV , respectively, and the compression modulus is 252 MeV . For comparison, the same saturation observables as predicted by the other DBHF model presently on the market³⁰ are 0.181 fm^{-3} and -16.15 MeV for saturation density and energy, and 230 MeV for the incompressibility.

The increased stiffness featured by the DBHF EoS at the higher densities originates from the strongly density-dependent repulsion inherent to the Dirac-Brueckner-Hartree-Fock method. In Ref.⁵¹, it is pointed out that constraints from neutron star phenomenology together with flow data from heavy-ion reactions suggest that such EoS behavior may be desirable. We will come back to this point later, in conjunction with neutron star predictions.

At this point, it is useful to take a closer look at some of the predictions included in the analysis of Ref.⁵¹, such as relativistic mean field (RMF) models. Examples are those from Refs.^{52,53}, which use density-dependent (“DD”) meson couplings and are fitted to the properties of nuclei up to about 0.15 fm^{-3} . They generate the steepest EoS and thus the largest pressures, see Fig. 5. An improvement to the traditional RMF description of nuclear matter can be obtained through the introduction of non-linear (“NL”) self-interactions of the σ meson, such as done in the models of Refs.^{54,55}, with the parametrization of Ref.⁵⁵ including both the δ and the ρ mesons in the isovector channel. The corresponding EoS are much

less repulsive than those of “DD” models (although the symmetry energy becomes very large at high density, possibly due to the absence of non-linearity and density dependence at the isovector level).

Clearly, the pressure as a function of density plays the crucial role in building the structure of a neutron star. In Fig. 6 we show the pressure in symmetric matter as predicted by the Idaho calculation compared with constraints obtained from flow data.⁵⁶ The predictions are seen to fall just on the high side of the constraints and grow rather steep at high density. Comparing with Fig. 5, we see that the Idaho predictions are well below those of DD-RMF models at low to moderate density but nearly catch up with them at very high density, a description that would also be appropriate for the DBHF predictions of Ref.³⁰ (red curve in Fig. 5). Of all the cases studied in Ref.⁵¹, DD-RMF models predict the largest maximum masses and radii and the lowest central densities. Thus, an equation of state where high pressure is sustained for a longer radial distance (moving away from the center of the star) will allow the maximum mass star to be heavier, larger, and more “diffuse” at the center. On the other hand, microscopic relativistic models, (such as the DBHF calculation of Ref.³⁰ or the present one, which are in fair agreement with each other), display a rather different density dependence of the pressure and produce smaller and more compact maximum mass stars. (All other EoS considered in Ref.⁵¹ are softer and generate smaller maximum masses with smaller radii and larger central densities.)

To conclude this section, we show in Fig. 7 the pressure in neutron matter (red curve) and β -equilibrated matter (green) as predicted by DBHF calculations. The pressure contour is again from Ref.⁵⁶ and was obtained from flow data together with the assumption of strong density dependence in the asymmetry term (indicated as “Asy_ stiff” in Ref.⁵⁶).

3.2.3. *The symmetry energy and related observables*

Here we will focus specifically on the symmetry energy and its impact on the structure of neutron-rich nuclei, in particular the neutron skin thickness.

In Fig. 8, we display the Idaho DBHF prediction for the symmetry energy by the solid red curve. The curve is seen to grow at a lesser rate with increasing density, an indication that, at large density, repulsion in the symmetric matter EoS increases more rapidly than in the neutron matter EoS. This can be understood in terms of increased repulsion in isospin zero partial waves (absent from neutron matter) as a function of density. Our predicted value for the symmetry pressure, L , (see Eq. (38) below), is 69.6 MeV.

The various black dashed curves in Fig. 4 are obtained with the simple parametrization

$$e_{sym} = C(\rho/\rho_0)^\gamma, \quad (36)$$

with γ increasing from 0.7 to 1.0 in steps of 0.1, and $C \approx 32$ MeV. It seems that

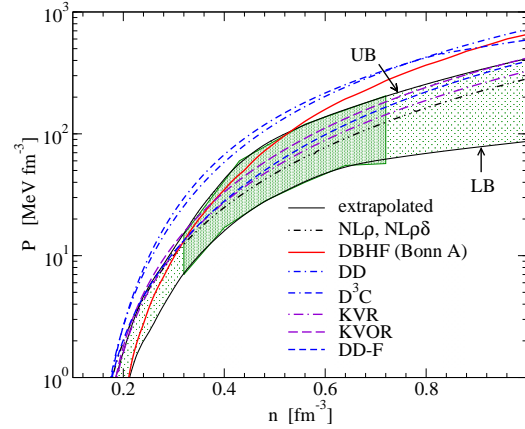


Fig. 5. Pressure in symmetric matter predicted by various models. The shaded area corresponds to the region of pressure consistent with the flow data analysed in Ref.⁵⁶. [Figure reprinted with permission from T. Klähn.⁵¹ Copyright (2006) by the American Physical Society. <http://prc.aps.org/abstract/PRC/v74/i3/e035802>]

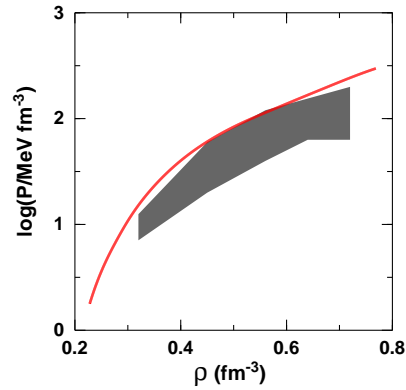


Fig. 6. Pressure in symmetric matter from the Idaho DBHF calculation. The shaded area corresponds to the region of pressure consistent with the flow data analysed in Ref.⁵⁶.

a value of γ close to 0.8 gives a reasonable description of the DBHF predictions, although the use of different functions in different density regions would be best for an optimal fit.

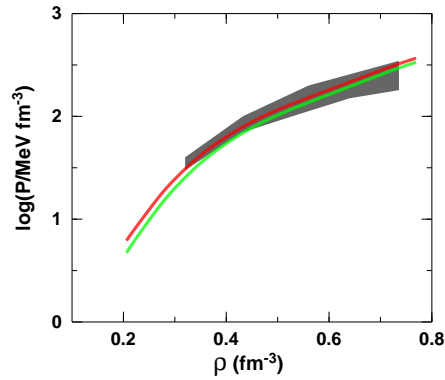


Fig. 7. Pressure in neutron (red curve) and baryon-lepton (green curve) matter from the Idaho DBHF calculation. The shaded area corresponds to the region of pressure consistent with flow data and the inclusion of strong density dependence in the asymmetry terms.⁵⁶

Considering that all of the dashed curves are commonly used parametrizations suggested by heavy-ion data,⁵⁷ Fig. 4 clearly reflects our limited knowledge of the symmetry energy, particularly, but not exclusively, at the larger densities.

As already mentioned in Sec. 2, from the experimental side intense effort is going on to obtain reliable empirical information for the less known aspects of the EoS. Heavy-ion reactions are a popular way to seek constraints on the symmetry energy, through analyses of observables that are sensitive to the pressure gradient between nuclear and neutron matter. Isospin diffusion data from heavy-ion collisions, together with analyses based on isospin-dependent transport models, can provide information on the slope of the symmetry energy.

Concerning the lower densities, isospin-sensitive observables can also be identified among the properties of normal nuclei. The neutron skin of neutron-rich nuclei is a powerful isovector observable, being sensitive to the slope of the symmetry energy, which determines to which extent neutrons will tend to spread outwards to form the skin. It is the purpose of this section to systematically examine and discuss the symmetry energy properties in microscopic models and the corresponding neutron skin predictions. We will take the skin of ^{208}Pb as our representative isovector “observable”.

Parity-violating electron scattering experiments are now a realistic option to determine neutron distributions with unprecedented accuracy. The neutron radius of ^{208}Pb is expected to be measured within 0.05 fm thanks to the electroweak program at the Jefferson Laboratory.⁵⁸ This level of accuracy could not be achieved with

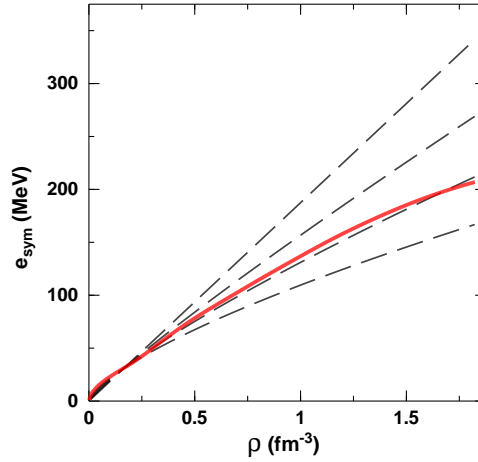


Fig. 8. DBHF prediction for the symmetry energy (solid red) compared with various phenomenological parametrizations (dashed black). See text for details.

hadronic scattering. Parity-violating electron scattering at low momentum transfer is especially suitable to probe neutron densities, as the Z^0 boson couples primarily to neutrons. With the success of this program, reliable empirical information on neutron skins will be able to provide, in turn, much needed *independent* constraint on the density dependence of the symmetry energy.

We form an energy functional based on the semi-empirical mass formula, where the volume and symmetry terms are contained in the isospin-asymmetric equation of state. Thus, we write the energy of a (spherical) nucleus as

$$E(Z, A) = \int d^3r e(\rho(r), \alpha(r))\rho(r) + \int d^3r f_0(|\nabla\rho(r)|^2 + \beta|\nabla\rho_I(r)|^2) + \text{Coulomb term}. \quad (37)$$

In the above equation, ρ and ρ_I are the usual isoscalar and isovector densities, given by $\rho_n + \rho_p$ and $\rho_n - \rho_p$, respectively, in terms of neutron and proton densities. α is the neutron asymmetry parameter, $\alpha = \rho_I/\rho$, and $e(\rho, \alpha)$ is the energy per particle in isospin-asymmetric nuclear matter. The latest Idaho EoS⁵⁹ will be used in Eq. (37), along with others from different models.

From fits to nuclear binding energies, the constant f_0 in Eq. (37) is approximately 70 MeV fm^5 , whereas the contribution of the term proportional to β was found to be minor.² Thus it is reasonable to neglect it. (The magnitude of β was estimated to be about 1/4 in Ref.³, where it was observed that, even with variations of β between -1 and +1, the effect of the β term on the neutron skin was negligibly

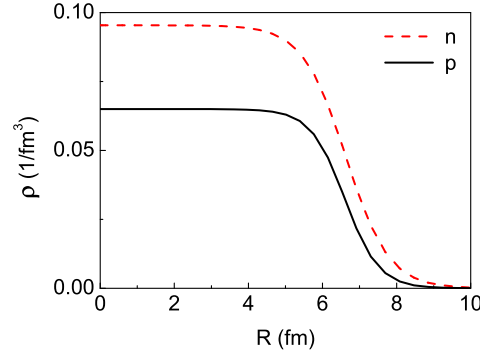


Fig. 9. (color online) Neutron (red) and proton (black) point densities as obtained from the DBHF model.

small.)

The parameters of the proton and neutron densities are obtained by minimizing the value of the energy functional, Eq. (37), assuming Thomas-Fermi distribution functions. Although simple, this method has the advantage of allowing a very direct connection between the EoS and the properties of finite nuclei. (It could be used, for instance, to determine a semi-phenomenological EoS by fitting it to both binding energies and charge radii of closed-shell nuclei.)

In Fig. 9, we show the proton and neutron Thomas-Fermi distributions for ^{208}Pb as obtained with the method described above and the DBHF model for the EoS. The predicted proton and neutron root-mean-square radii are 5.39 fm and 5.56 fm, respectively.

Typically, predictions of the symmetry energy at saturation density encountered in the literature are in reasonable agreement with one another, ranging approximately from 26 to 35 MeV. On the other hand, the slope of the symmetry energy is more model dependent and less constrained. This is seen through the symmetry pressure, defined as

$$L = 3\rho_0 \left(\frac{\partial e_{\text{sym}}(\rho)}{\partial \rho} \right)_{\rho_0} \approx 3\rho_0 \left(\frac{\partial e_{n.m.}(\rho)}{\partial \rho} \right)_{\rho_0}. \quad (38)$$

Thus, L is sensitive to the gradient of the energy per particle in neutron matter ($e_{n.m.}$). As to be expected on physical grounds, the neutron skin, given by

$$S = \sqrt{\langle r_n^2 \rangle} - \sqrt{\langle r_p^2 \rangle}, \quad (39)$$

is highly sensitive to the same gradient.

Values of L are reported to range from -50 to 100 MeV as seen, for instance, through the numerous parametrizations of Skyrme interactions (see Ref.⁵⁷ and references therein), all chosen to fit the binding energies and the charge radii of a large number of nuclei. Heavy-ion data impose boundaries for L at 85 ± 25 MeV,^{60,61}

with more stringent constraints being presently extracted.³³ Other reports³⁹ state the constraints as 85 ± 55 MeV. Also, a nearly linear correlation is observed between the neutron skin S and the L parameter.⁶²

Such phenomenological studies are extremely useful, but, ultimately, they must be compared with *ab initio* approaches in order to get true physical insight. The direct connection with the underlying nuclear forces will then facilitate the physical understanding, when combined with reliable constraints.

As explained in Sec. 3.2.1, the DBHF model does not include three-body forces explicitly, but effectively incorporates the class of TBF originating from the presence of nucleons and antinucleons (the “Z-diagrams” in Fig. 2), see previous discussion. As the other main input of our comparison, we will take the EoS from the microscopic approach of Ref.⁴⁹. There (and in previous work by the same authors), the Brueckner-Hartree-Fock (BHF) formalism is employed along with microscopic three-body forces. In particular, in Ref.⁶³ the meson-exchange TBF are constructed applying the same parameters as used in the corresponding nucleon-nucleon (NN) potentials, which are: Argonne V18⁶⁴ (V18), Bonn B¹ (BOB), Nijmegen 93⁶⁵ (N93). The popular (but phenomenological) Urbana TBF⁶⁶ (UIX) is also utilized in Ref.⁶³. Convenient parametrizations in terms of simple analytic functions are given in all cases and we will use those to generate the various EoS. We will refer to this approach, generally, as “BHF + TBF”. This comparison will bring up the discussion on microscopic models and explicit TBF outlined in Sec. 3.2.

In Fig. 10, we display Idaho DBHF predictions for the symmetry energy, solid black curve, along with those from V18, BOB, UIX, and N93. All values of the symmetry energy at the respective saturation densities are between 29 and 34 MeV. A larger spreading is seen in the L parameter, see left panel of Fig. 11, where the values range from about 70 to 106 MeV. The respective neutron skin predictions are shown on the vertical axis.

We notice that all BHF+TBF models predict larger L , and thus larger neutron skins, as compared with DBHF, corresponding to a faster growth of the energy per particle in neutron matter relative to symmetric matter. This can be seen from Fig. 10, especially for the higher densities. The present calculations reveal that there are more subtle, but significant differences at low to medium densities as well.

Some comments are in place concerning the nature of the L vs. S correlation. If a family of models is constructed so that they differ *mostly* in the slope of the symmetry energy, a linear correlation may be expected among L and the skin.⁶² The models we are considering, however, differ from one another in more than just the slope of the symmetry energy. Thus, although the general pattern is that a larger L corresponds to a larger skin, the relation is more complex, as the r.m.s. radius of the neutron distribution will, to some extent, receive feedback from the smaller or larger degree of attraction that binds neutrons and protons, and which depends on the symmetric matter EoS.

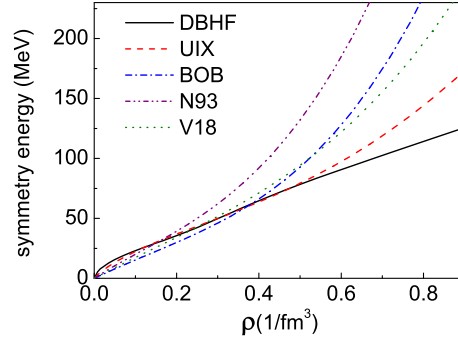


Fig. 10. (color online) Predictions for the symmetry energy from DBHF and various “BHF + TBF” models discussed in the text.

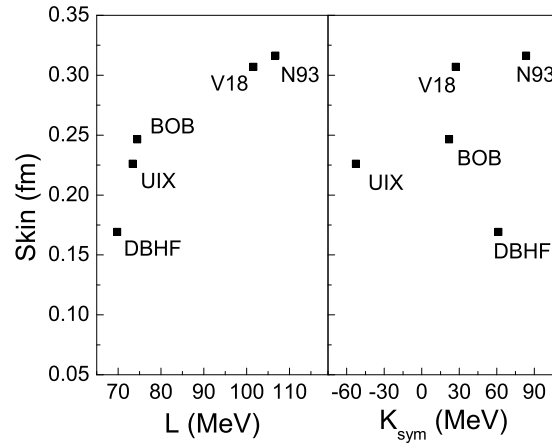


Fig. 11. Left panel: neutron skin of ^{208}Pb vs. the symmetry pressure for the models considered in the text; Right panel: neutron skin of ^{208}Pb vs. the curvature of the symmetry energy, K_{sym} , for the same models.

The next term in the expansion of the symmetry energy is the K_{sym} parameter,

$$K_{sym} = 9\rho_0^2 \left(\frac{\partial^2 e_{sym}(\rho)}{\partial \rho^2} \right)_{\rho_0}, \quad (40)$$

which is a measure for the curvature of the symmetry energy. The neutron skin *vs.* K_{sym} is shown in the right panel of Fig. 11 for the various models. Although the values of K_{sym} appear more spread out, the large negative values obtained with some of the parametrizations of the Skyrme model are not present. Those large negative values (as low as -600 MeV) produced by Skyrme models indicate a strongly downward curvature of the symmetry energy already at low to medium densities. We also notice from Fig. 11 (right panel) that no clear correlation can be

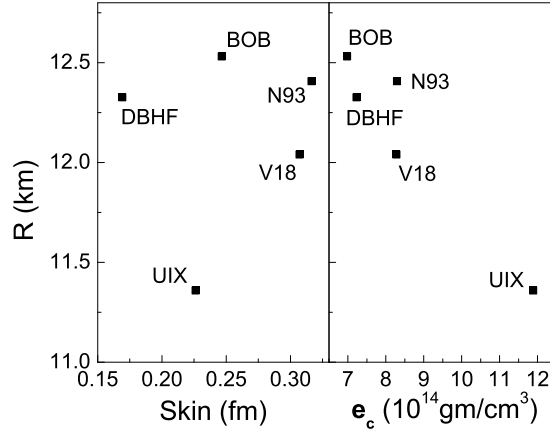


Fig. 12. Left panel: neutron skin of ^{208}Pb vs. the radius of a $1.4M_\odot$ neutron star for the models considered in the text. Right panel: star radius vs. the central energy density for the same models.

identified between K_{sym} and the neutron skin.

We conclude this section by showing in Fig. 12 the relation between the neutron skin of ^{208}Pb and the radius of a $1.4M_\odot$ neutron star for the models we are considering. (A more detailed discussion of neutron stars and the EoS will be presented in Sec. 4.) Stellar matter contains neutrons in β equilibrium with protons, electrons, and muons. Tabulated values for the latest Idaho DBHF EoS can be found later in this article. We have applied β -stability in the same way to all the various models of Ref.⁶³ starting from the given parametrized versions of the respective symmetric matter and neutron matter EoS. For the case of leptons, typically treated as a gas of non-interacting fermions, the equations of β -stability (which amount to imposing energy conservation and charge neutrality), are elementary to solve (see Sec. 4.2).

At subnuclear densities, all the EoS considered here are joined with the crustal equations of state from the work of Harrison and Wheeler⁶⁷ (for energy densities between 10 and $10^{11} \text{ g cm}^{-3}$) and the work of Negele and Vautherin⁶⁸ (for energy densities less than $1.7 \times 10^{13} \text{ g cm}^{-3}$).

At first, Fig. 12 can appear surprising, since it shows that larger skin does not necessarily imply larger radius. On the other hand, one must keep in mind that, as we argued previously, these models differ from one another in more than just the slope of the symmetry energy. Furthermore, the star radius probes higher densities than the skin does. Generally, if a family of models is constructed so that they differ *mostly* in the slope of the symmetry energy, a linear correlation is expected among L , the skin, and R .⁶⁹

In summary: Most models agree on the value of the symmetry energy around the saturation point within a few MeV, but we are far from a reasonable agreement on its derivative and even farther from agreement on its curvature. Although mi-

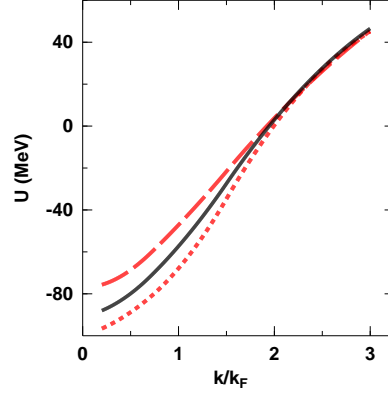


Fig. 13. The neutron (dashed line) and proton (dotted) single-particle potentials as a function of the momentum at fixed average density and $\alpha=0.4$. The solid curve in the middle is the single-nucleon potential at $\alpha=0$.

microscopic models do not display as much spread as phenomenological ones, a point that comes out clearly from the present study is that a measurement of the neutron skin of ^{208}Pb with an accuracy of 0.05 fm, as it has been announced,⁷⁰ should definitely be able to discriminate among the EoS from these microscopic models.

3.2.4. Neutron and proton single-particle properties and the symmetry potential

In this section we will concentrate specifically on predictions of isovector single-particle properties, such as the neutron and proton single-particle potentials and the closely related symmetry potential. These “observables” depend sensitively on the difference between neutron and proton properties in asymmetric matter and play an important role in simulations of heavy-ion collisions with neutron-rich nuclei.

In terms of the G -matrix, calculated as described in Sec. 3.2.1, we write the single-nucleon potential (in the case of unequal Fermi levels for protons and neutrons), as

$$U_i(k) = \text{Re} \left[\sum_{q < k_F^p} \langle kq | G_{in} | kq - qk \rangle + \sum_{q < k_F^p} \langle kq | G_{ip} | kq - qk \rangle \right], \quad (41)$$

where $i = n/p$ for neutron/proton, and k refers to states below and above the Fermi momentum (consistent with the “continuous choice” for the single-particle spectrum).

We begin by examining the momentum dependence of $U_{n/p}$, the single neutron/proton potential in neutron-rich matter. In Fig. 13, we show $U_{n/p}$ as a function of the momentum and a fixed value of the asymmetry parameter, $\alpha = 0.4$. The middle curve shows $U_n = U_p$ at $\alpha = 0$. The total nucleon density considered in the

figure is equal to 0.185 fm^{-3} and corresponds to a Fermi momentum of 1.4 fm^{-1} , which is very close to our predicted saturation density.

For increasing values of α (obviously, $U_n = U_p$ for $\alpha=0$), the proton potential becomes more attractive while the opposite tendency is observed in U_n . This reflects the fact that the proton-neutron interaction, the one predominantly felt by the single proton as the proton density is depleted, is more attractive than the one between identical nucleons. Also, as it appears reasonable, the dependence on α becomes weaker at larger momenta.

The role of the momentum dependence of the symmetry potential in heavy-ion collisions was examined and found to be important. Symmetry potentials with and without momentum dependence can lead to significantly different predictions of collision observables.⁷¹ More recently, these issues have been revisited in hot asymmetric matter.^{72,73}

Regarding $U_{n/p}$ as functions of the asymmetry parameter α , one can easily verify that the following approximate relation applies:

$$U_{n/p}(k, k_F, \alpha) \approx U_{n/p}(k, k_F, \alpha = 0) \pm U_{sym}(k, k_F) \alpha, \quad (42)$$

with the \pm referring to neutron/proton, respectively. Figure 14 displays the left-hand side of Eq. (42) for fixed density and nucleon momentum and clearly reveals the linear behaviour of $U_{n/p}$ as a function of α . Thus, one can expect isospin splitting of the single-particle potentials to be effective in separating the collision dynamics of neutrons and protons. Although the main focus of Fig. 14 is the α dependence, predictions are displayed for three different potentials, Bonn A,¹ B,¹ and C.¹ These three models differ mainly in the strength of the tensor force, which is mostly carried by partial waves with isospin equal to 0 and thus should fade away in the single-neutron potential as the neutron fraction increases. In fact, the figure demonstrates reduced differences among the values of U_n predicted with the three potentials at large α .

Already several decades ago, it was pointed out that the real part of the nuclear optical potential depends on the asymmetry parameter as in Eq. (42).⁷⁴ Then, the quantity

$$\frac{U_n + U_p}{2} = U_0, \quad (43)$$

which is obviously the single-nucleon potential in absence of asymmetry, should be a reasonable approximation to the isoscalar part of the optical potential in the interior of a nucleus. The momentum dependence of U_0 (which is shown in Fig. 13 as the $\alpha=0$ curve), is important for extracting information about the symmetric matter EoS and is reasonably agreed upon.^{75,76,77,78,79,80,81,82}

On the other hand,

$$\frac{U_n - U_p}{2\alpha} = U_{sym} \quad (44)$$

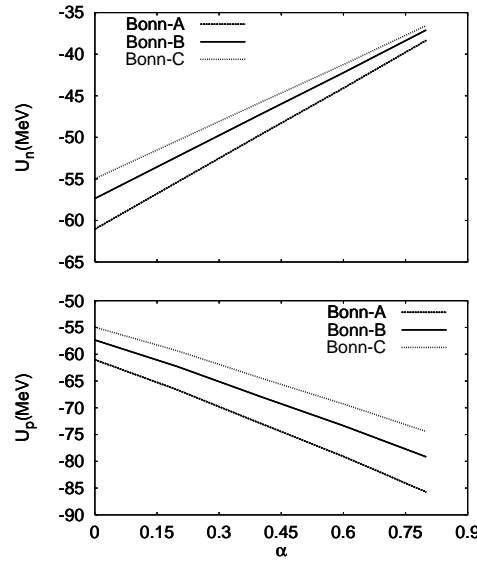


Fig. 14. The neutron and proton single-particle potentials as a function of the asymmetry parameter at fixed average density and momentum equal to the average Fermi momentum.

should be comparable with the Lane potential,⁷⁴ or the isovector part of the nuclear optical potential. (In the two equations above the dependence upon density, momentum, and asymmetry has been suppressed for simplicity.) We have calculated U_{sym} as a function of the momentum, or rather the corresponding kinetic energy. The predictions obtained with Bonn B are shown in Fig. 15. They are compared with the phenomenological expression⁷⁴

$$U_{Lane} = a - bT, \quad (45)$$

where T is the kinetic energy, $a \approx 22 - 34 \text{ MeV}$, $b \approx 0.1 - 0.2 \text{ MeV}$.

We observe that the strength of the (DBHF) predicted symmetry potential decreases with energy, a behavior which is consistent with the empirical information. The same comparison is done in Ref.⁸³ starting from a phenomenological formalism for the single-nucleon potential.^{84,85} There, it is shown that it is possible to choose two sets of parameters which lead to similar values of the symmetry energy but exactly opposite tendencies in the energy dependence of the symmetry potential as well as opposite sign of the proton-neutron mass splitting. As a consequence of that, these two sets of parameters lead to very different predictions for observables in heavy-ion collisions induced by neutron-rich nuclei.⁸⁵ This fact suggests that constraints from “differential” observables, namely those specifically sensitive to

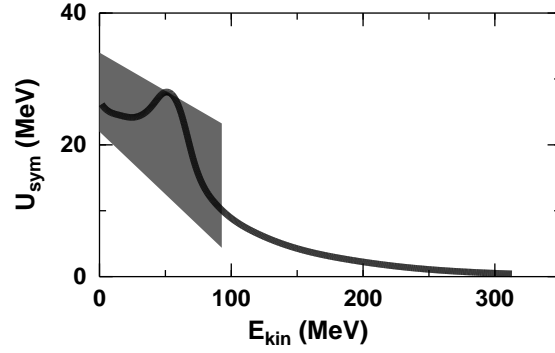


Fig. 15. The symmetry potential close to saturation density.

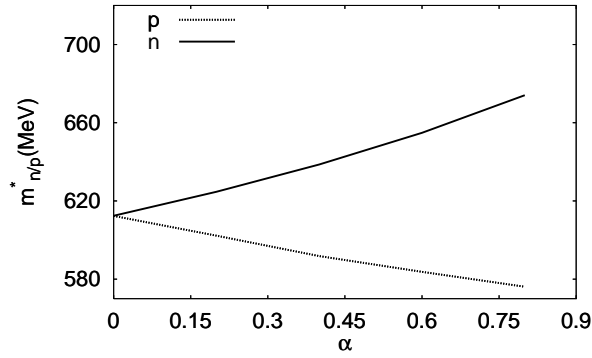


Fig. 16. The neutron and proton effective mass as a function of the asymmetry parameter at fixed average density.

the difference between proton and neutron properties in asymmetric matter, are very much needed.

The effective masses for proton and neutron corresponding to the single-nucleon potentials of Fig. 13 are shown in Fig. 16 as a function of α . The predicted effective mass of the neutron being larger than the proton's is a trend shared with microscopic non-relativistic calculations.⁸⁶ In the non-relativistic case, one can show from

Table 1. np total effective cross sections in symmetric matter calculated with various many-body models, see text for details.

$k_F(fm^{-1})$	$q_0(MeV)$	$\sigma_{np}^{DBHF}(mb)$	$\sigma_{np}^{BHF+TBF}(mb)$	$\sigma_{np}^{BHF}(mb)$
1.1	250	34.38	44.65	51.74
1.1	300	23.14	29.01	31.85
1.1	350	20.63	23.56	25.62
1.4	250	26.74	31.25	39.82
1.4	300	17.26	25.28	30.96
1.4	350	16.77	21.17	25.23
1.7	250	17.20	19.03	29.12
1.7	300	15.06	17.59	25.02
1.7	350	12.33	13.99	21.04

elementary arguments based on the curvature of the (parabolic) single-particle potential that a more attractive potential, as the one of the proton, leads to a smaller effective mass. In the DBHF quasi-particle approximation described in Sec. 3.2.1, one assumes momentum-independent nucleon self-energies, U_S and U_V , with a vanishing spacial component of the vector part. In such limit, the “Dirac mass” and the non-relativistic or “Landau mass” should coincide to leading order in the expansion of the relativistic single-particle potential.³⁰ It is therefore not surprising that our proton and neutron effective masses, although defined as Dirac masses ($m_i^* = m + U_{S,i}$), display a trend that is similar to the one generally expected in the non-relativistic case. Most likely, the main reason for the discrepancy in the predicted isospin mass splitting between the Idaho DBHF calculation and the DBHF model from Ref.³⁰ is in the way the scalar and vector fields are treated, particularly their momentum dependence.

Closely related to the effective mass is the concept of in-medium effective cross section. Transport equations, such as the Boltzmann-Uehling-Uhlenbeck equation, describe the evolution of a non-equilibrium gas of strongly interacting hadrons drifting in the presence of the mean field while undergoing two-body collisions. Thus heavy ion collision simulations require the knowledge of in-medium two-body cross sections as well as the mean field. Both should be calculated microscopically and self-consistently starting from the basic nuclear forces⁸⁷ and are closely related to the EoS.

To be fully applicable throughout the evolution of the colliding system, where high densities may be involved, in-medium cross sections must go beyond the conventional BHF. Although an extensive discussion of in-medium cross sections will not be presented here, we show in Tables 1 and 2 a comparison of the latest Idaho (DBHF) in-medium cross sections and those obtained from the BHF+TBF model of Lombardo *et al.*⁸⁷

We recall that the relativistic elastic differential cross section is calculated from

$$\sigma(\theta) = \frac{(m^*)^4}{4\pi^2 \hbar^4 s^*} |G(\theta)|^2, \quad (46)$$

Table 2. As in the previous Table, for identical particles.

$k_F(fm^{-1})$	$q_0(MeV)$	$\sigma_{NN}^{DBHF}(mb)$	$\sigma_{NN}^{BHF+TBF}(mb)$	$\sigma_{NN}^{BHF}(mb)$
1.1	250	18.00	18.15	22.98
1.1	300	16.41	17.47	19.48
1.1	350	17.08	18.55	19.51
1.4	250	15.72	13.74	19.76
1.4	300	13.70	14.43	17.23
1.4	350	16.31	16.89	19.46
1.7	250	18.05	7.87	13.36
1.7	300	17.93	9.98	13.98
1.7	350	13.96	11.48	16.43

where $s^* = 4((m^*)^2 + \vec{q}^2)$. Notice that the relativistic amplitude, G , is related to the non-relativistic one through $G = \frac{E^*}{m^*} G_{n.r.}$, with $E^* = ((m^*)^2 + \vec{q}^2)^{1/2}$.

In Tables 1 and 2, q_0 signifies the momentum of either nucleon in their center-of-mass frame, for simplicity assumed to coincide with the nuclear matter rest frame. The 4th and 5th columns show the results obtained by Lombardo *et al.* with BHF calculations implemented or not with TBF. There is generally a fair amount of agreement between the DBHF and the BHF+TBF results. For the np case, energy and density dependence appear consistent among the two sets of results displayed in columns 3 and 4, although the BHF+TBF results are generally larger. For the case of identical nucleons, the DBHF values are in good agreement with those from BHF+TBF, with the exception of the highest densities. This is to be expected in view of the larger differences existing between the DBHF and the BHF+TBF predictions of the EoS at high density.

Besides being a crucial part of the input for transport models, in-medium effective cross sections are important in their own right as they allow to establish an immediate connection with the nucleon mean free path, λ , one of the most fundamental properties characterizing the propagation of nucleons through matter.⁸⁸ It can be written as

$$\lambda = \frac{1}{\sigma_{pp}\rho_p + \sigma_{pn}\rho_n}, \quad (47)$$

for a proton propagating through matter with proton and neutron densities equal to ρ_p and ρ_n , respectively. The mean free path enters the calculation of the nuclear transparency function, which is the probability that the projectile will pass through the target without interacting. This is closely related to the total reaction cross section of a nucleus, which can be used to extract nuclear r.m.s. radii within Glauber models.⁸⁹ Therefore, microscopic in-medium isospin-dependent NN cross sections can ultimately help obtain information about the properties of exotic, neutron-rich nuclei, such as, for instance, the target density. The latter is a very useful information, especially for exotic nuclei or nuclei with large neutron skins (where densities cannot be probed with conventional charged lepton scattering).

4. Neutron Star Properties

Proceeding in our review of the various systems and phenomena where the EoS plays a chief role, we will now take a look at some of the most exotic systems in the universe, compact stars.

4.1. *A brief review of neutron star structure and available constraints*

Neutron stars are stable configurations containing the most dense form of matter found in the universe. They are therefore unique laboratories to study the properties of highly compressed (cold) matter. Furthermore, the possibility of exploring the structure of neutron stars via gravitational waves⁹⁰ makes these exotic objects even more exciting.

The densities found in neutron stars range from the density of iron to several times normal nuclear density. In the low-density region, matter is highly compressed and fully ionized and consists of electrons and ions of iron. As density increases, charge neutrality requires matter to become more neutron rich. In this density range ($10^7 \leq \rho \leq 10^{11} \text{ g cm}^{-3}$), neutron-rich nuclei appear, such as isotopes of ^{62}Ni , ^{86}Kr , ^{84}Se , ^{80}Zn , ^{124}Mo , ^{122}Zr . Above densities of approximately $10^{11} \text{ g cm}^{-3}$, free neutrons begin to form a continuum of states. The inner crust is then a compressed solid with a fluid of neutrons. At densities equal to approximately 1/2 of saturation density, clusters begin to merge into a continuum. In this phase, matter is a uniform fluid of neutrons, protons, and leptons. Protons and neutrons can condense in superfluids and superconducting states below temperatures of about 10^9 K .⁹¹ Above a few times nuclear matter density, the actual composition of stellar matter is not known. Strange baryons can appear when the nucleon chemical potential is of the order of their rest mass. We will address the issue of strange matter later in this article. At even higher densities, transitions to other phases are speculated, such as a deconfined, rather than hadronic, phase. The critical density for such transition cannot be predicted reliably because it lies in a range where QCD is non perturbative.⁹¹

Recently, a semi-algebraic expression for the EoS of cold quark matter has been derived within the Dyson-Schwinger formalism.⁹² The Dyson-Schwinger framework can address both confinement and dynamical chiral symmetry breaking,⁹² unlike other models commonly used in conjunction with cold quark matter, such as the Nambu-Jona-Lasinio model or bag-type models. It will be interesting to see applications of the model described in Ref.⁹² to dense astrophysical systems. For that purpose, the quark matter EoS will need to be supplemented by the nuclear matter EoS. In the meantime, it is encouraging that the model predicts coincident deconfinement and chiral symmetry restoring transitions.

The possibility has been speculated that the most stable state at zero pressure may be u , d , s quark matter instead of iron. This would imply that strange quark matter is the most stable (in fact, the absolutely stable) state of strongly interacting

matter, as originally proposed by Bodmer,⁹³ Witten,⁹⁴ and Terazawa.⁹⁵ In such case, hyperonic and hybrid stars would have to be metastable with respect to stars composed of stable three-flavor strange quark matter,⁹⁶ which is lower in energy than two-flavor quark matter due to the extra Fermi levels open to strange quarks. Whether or not strange quark stars can give rise to pulsar glitches, (which are observed sudden small changes in the rotational frequency of a pulsar), may be a decisive test of the strange quark matter hypothesis.⁹⁶

The maximum mass and the radius of a neutron star are sensitive to different aspects of the EoS. The maximum mass is mostly determined by the stiffness of the EoS at densities greater than a few times saturation density. Non-nucleonic degrees of freedom, which typically make their appearance at those densities, are known to have a considerable impact on the maximum mass of the star. Causality imposes a limit of about 3 solar masses to the maximum mass, the existence of which is inherent to general relativity and is predicted by the equation of hydrostatic equilibrium,

$$\frac{dP(r)}{dr} = -\frac{G}{c^2} \frac{(P(r) + \epsilon(r))(M(r) + 4\pi r^3 P(r)/c^2)}{r(r - 2GM(r)/c^2)}, \quad (48)$$

with

$$\frac{dM(r)}{dr} = 4\pi^2 \rho(r), \quad (49)$$

where ϵ is the total mass-energy density. The pressure is related to the energy/particle through

$$P(\rho) = \rho^2 \frac{\partial e(\rho)}{\partial \rho}. \quad (50)$$

It's worth recalling that no mass limit exists in Newtonian gravitation.

The star radius is mainly sensitive to the slope of the symmetry energy. In particular, it is closely connected to the internal pressure (that is, the energy gradient) of matter at densities between about $1.5\rho_0$ and $2\text{--}3\rho_0$.⁹⁷

Lattimer and Prakash investigated the maximum central density question.⁹⁷ Combining the causality limit ($R \geq 2.87GM/c^2$) with the central density-mass relation implied by the Tolman VII solution,⁹⁸

$$\rho = \rho_c(1 - r^2/R^2), \quad (51)$$

they obtained the relation

$$\rho_c M^2 \leq 15.3 \times 10^{15} M_\odot^2 g \text{ cm}^{-3}. \quad (52)$$

The maximum gravitational mass and the corresponding radius are the typical observables used to constraint the EoS. Much more stringent constraints could be imposed on EoS if these two quantities could be determined independently from each other. At this time, the heaviest neutron star (with accurately known mass) has a mass of $1.671 \pm 0.008 M_\odot$,⁹⁹ but neutron stars with masses above 2 solar

masses are expected to exist.¹⁰⁰ Mass limits are obtained from observations of binary systems, either a two-neutron star system or a neutron star and a massive companion, such as a white dwarf. The pulsar in the Hulse-Taylor binary system¹⁰⁰ has a mass of $1.4408 \pm 0.0003 M_{\odot}$, to date the best mass determination.

Measurements of the radius are considerably less precise than mass measurements.⁹⁷ The radiation or photospheric radius, R_{∞} , is related to the actual stellar radius by $R_{\infty} = R(1 - R/R_S)^{-1/2}$, where $R_S = 2GM/R$ is the Schwarzschild radius. Estimates are usually based on thermal emission of cooling stars, including redshifts, and the properties of sources with bursts or thermonuclear explosions at the surface.

Neutrinos are also used as a probe of the EoS. Neutrino luminosity is controlled by several factors including the total mass of the (proton-neutron) star and the opacity of neutrinos at high densities, which of course is sensitive to the EoS of dense matter.

Gravitational waves⁹⁰ are a less conventional way to probe neutron star properties. Emission of gravitational waves causes orbital decay, the observation of which would allow an estimate of the moment of inertia and thus, together with an accurate measurement of the mass, impose stronger boundaries on the EoS. A measurement of the moment of inertia within 10%, together with the information on the mass, would be able to discriminate among various EoS.⁹⁷ To date, the best determination of the moment of inertia is the one for the Crab pulsar¹⁰¹ which would rule out only very soft EoS.⁹⁷

The minimum mass of a neutron star is also a parameter of interest. For a cold, stable system, the minimum mass is about $0.09 M_{\odot}$.⁹⁷ The smallest reliably estimated neutron star mass is the companion of the binary pulsar J1756-2251, which has a mass of $1.18 \pm 0.02 M_{\odot}$.¹⁰²

4.2. *Comparing predictions of microscopic models*

As constraints from nuclear physics and/or astrophysics promise to become more stringent, it is important to understand and compare how the nature of the various predictions is related to the features of each model. In microscopic approaches, the tight connection with the underlying forces facilitates physical interpretation of the predictions in terms of the characteristics of the nuclear force and its behavior in the medium. Motivated by these considerations, in this section we calculate several neutron star properties, for static and/or rotating stars, using equations of state based on different microscopic models. These will be the same as those used in Sec. 3.2.3 to examine symmetry energy and neutron skin predictions, namely BOB, V18, N93, and UIX, along with Idaho DBHF.

In Sec. 3.2.3, we compared the predictions of the neutron skin in ^{208}Pb by these models and correlated them with differences in the slope of the symmetry energy. Model differences become larger at high-density and will naturally impact neutron star predictions.

Table 3. DBHF equation of state of pure neutron matter.

Baryon density($1/cm^3$)	Energy density(g/cm^3)	Pressure($dyne/cm^2$)
0.145902E+38	0.245257E+14	0.434992E+32
0.231688E+38	0.389881E+14	0.874118E+32
0.345843E+38	0.582634E+14	0.156362E+33
0.492421E+38	0.830558E+14	0.257664E+33
0.675475E+38	0.114075E+15	0.468635E+33
0.781946E+38	0.132151E+15	0.621198E+33
0.899057E+38	0.152061E+15	0.816935E+33
0.102731E+39	0.173905E+15	0.111487E+34
0.116722E+39	0.197791E+15	0.156721E+34
0.131929E+39	0.223833E+15	0.223210E+34
0.148402E+39	0.252158E+15	0.319807E+34
0.166192E+39	0.282905E+15	0.463315E+34
0.185350E+39	0.316247E+15	0.681545E+34
0.205927E+39	0.352381E+15	0.993009E+34
0.227973E+39	0.391534E+15	0.141505E+35
0.251538E+39	0.433969E+15	0.203050E+35
0.276674E+39	0.480078E+15	0.293314E+35
0.303432E+39	0.530247E+15	0.409031E+35
0.331861E+39	0.584918E+15	0.558832E+35
0.362012E+39	0.644589E+15	0.746722E+35
0.393937E+39	0.709762E+15	0.965629E+35
0.427685E+39	0.780907E+15	0.122694E+36
0.463308E+39	0.858621E+15	0.152765E+36
0.500856E+39	0.943372E+15	0.185795E+36
0.540380E+39	0.103570E+16	0.223317E+36
0.581930E+39	0.113630E+16	0.268106E+36
0.625557E+39	0.124615E+16	0.324163E+36
0.671312E+39	0.136650E+16	0.395072E+36
0.719245E+39	0.149890E+16	0.485417E+36
0.769408E+39	0.164502E+16	0.589746E+36
0.821850E+39	0.180610E+16	0.707244E+36
0.876622E+39	0.198388E+16	0.846053E+36
0.933776E+39	0.218030E+16	0.100924E+37
0.993361E+39	0.239765E+16	0.120127E+37
0.105543E+40	0.263842E+16	0.142307E+37
0.112003E+40	0.290521E+16	0.167838E+37
0.118721E+40	0.320102E+16	0.197388E+37
0.125703E+40	0.352921E+16	0.231442E+37
0.132954E+40	0.389345E+16	0.270588E+37
0.140478E+40	0.429785E+16	0.315475E+37
0.148280E+40	0.474691E+16	0.366826E+37
0.156366E+40	0.524560E+16	0.425495E+37
0.164741E+40	0.579940E+16	0.492059E+37
0.173410E+40	0.641418E+16	0.567978E+37
0.182378E+40	0.709679E+16	0.654219E+37

As mentioned in Sec. 3.2.3, at subnuclear densities all the EoS considered here are joined with the crustal equations of state from Harrison and Wheeler⁶⁷ and Negele and Vautherin.⁶⁸ The composition of the crust is crystalline, with light⁶⁷

Table 4. As in the previous Table, for β -equilibrated matter.

Baryon density($1/cm^3$)	Energy density(g/cm^3)	Pressure($dyne/cm^2$)
0.145902E+38	0.245236E+14	0.416322E+32
0.231688E+38	0.389827E+14	0.822804E+32
0.345843E+38	0.582501E+14	0.142104E+33
0.492421E+38	0.830269E+14	0.230061E+33
0.675475E+38	0.114019E+15	0.409814E+33
0.781946E+38	0.132073E+15	0.540126E+33
0.899057E+38	0.151955E+15	0.711724E+33
0.102731E+39	0.173765E+15	0.970498E+33
0.116722E+39	0.197605E+15	0.137046E+34
0.131929E+39	0.223589E+15	0.201627E+34
0.148402E+39	0.251837E+15	0.261928E+34
0.166192E+39	0.282481E+15	0.330297E+34
0.185350E+39	0.315683E+15	0.517205E+34
0.205927E+39	0.351619E+15	0.757028E+34
0.227973E+39	0.390495E+15	0.110037E+35
0.251538E+39	0.432555E+15	0.160843E+35
0.276674E+39	0.478138E+15	0.235092E+35
0.303432E+39	0.527601E+15	0.334557E+35
0.331861E+39	0.581355E+15	0.465834E+35
0.362012E+39	0.639861E+15	0.632143E+35
0.393937E+39	0.703594E+15	0.832228E+35
0.427685E+39	0.773030E+15	0.107139E+36
0.463308E+39	0.848703E+15	0.134775E+36
0.500856E+39	0.931088E+15	0.165606E+36
0.540380E+39	0.102069E+16	0.200271E+36
0.581930E+39	0.111814E+16	0.241417E+36
0.625557E+39	0.122434E+16	0.293125E+36
0.671312E+39	0.134047E+16	0.358691E+36
0.719245E+39	0.146797E+16	0.442173E+36
0.769408E+39	0.160841E+16	0.539098E+36
0.821850E+39	0.176298E+16	0.649283E+36
0.876622E+39	0.193337E+16	0.779667E+36
0.933776E+39	0.212141E+16	0.932987E+36
0.993361E+39	0.232930E+16	0.111395E+37
0.105543E+40	0.255941E+16	0.132452E+37
0.112003E+40	0.281437E+16	0.156916E+37
0.118721E+40	0.309721E+16	0.185697E+37
0.125703E+40	0.341144E+16	0.219046E+37
0.132954E+40	0.376060E+16	0.257227E+37
0.140478E+40	0.414881E+16	0.301377E+37
0.148280E+40	0.458067E+16	0.352202E+37
0.156366E+40	0.506130E+16	0.410655E+37
0.164741E+40	0.559636E+16	0.477543E+37
0.173410E+40	0.619202E+16	0.554149E+37
0.182378E+40	0.685522E+16	0.641233E+37

or heavy⁶⁸ metals and electron gas. The DBHF equations of state for neutron matter and for β -equilibrated matter are given in Table 3 and Table 4, respectively. Some points of the EoS used for the crust are displayed in Table 5.

Table 5. Equation of state used for the crust. See text for details.

Baryon density($1/cm^3$)	Energy density(g/cm^3)	Pressure($dyne/cm^2$)
0.59701000E+25	0.99998600E+01	0.40721410E+12
0.19099900E+26	0.31992190E+02	0.47174340E+14
0.38376300E+26	0.64279760E+02	0.33550870E+15
0.15492600E+27	0.25949850E+03	0.88776630E+16
0.31128200E+27	0.52139300E+03	0.38114990E+17
0.62543700E+27	0.10476010E+04	0.15215920E+18
0.25249000E+28	0.42291870E+04	0.20992040E+19
0.50731100E+28	0.84974150E+04	0.74261220E+19
0.20480200E+29	0.34304300E+05	0.87378890E+20
0.41149300E+29	0.68925200E+05	0.29327530E+21
0.13164600E+30	0.22050990E+06	0.21592540E+22
0.26450500E+30	0.44305570E+06	0.70850350E+22
0.53144400E+30	0.89020260E+06	0.23123900E+23
0.21453100E+31	0.35937570E+07	0.19523170E+24
0.43102100E+31	0.72207080E+07	0.54232090E+24
0.13787700E+32	0.23100980E+08	0.28166750E+25
0.34951600E+32	0.58569360E+08	0.10057550E+26
0.70215700E+32	0.11767960E+09	0.25560490E+26
0.28334500E+33	0.47507410E+09	0.15831900E+27
0.56915000E+33	0.95453350E+09	0.38815460E+27
0.22959600E+34	0.38534730E+10	0.22901680E+28
0.46107400E+34	0.77425110E+10	0.55287600E+28
0.14734400E+35	0.24770450E+11	0.23888140E+29
0.29580200E+35	0.49769610E+11	0.57354730E+29
0.59374600E+35	0.99998600E+11	0.13755860E+30
0.30685800E+36	0.51813430E+12	0.66738040E+30
0.60373600E+36	0.10203670E+13	0.12773240E+31
0.10985200E+37	0.18580330E+13	0.20087290E+31
0.15931600E+37	0.26960450E+13	0.26615840E+31
0.19888300E+37	0.33666280E+13	0.32106350E+31
0.23844100E+37	0.40373370E+13	0.38075420E+31
0.26810600E+37	0.45404400E+13	0.42918160E+31
0.29776600E+37	0.50436140E+13	0.48089980E+31
0.32742200E+37	0.55468420E+13	0.53594420E+31
0.35707300E+37	0.60501410E+13	0.59429390E+31
0.38672000E+37	0.65534760E+13	0.65589600E+31
0.41636500E+37	0.70568810E+13	0.72068480E+31
0.44600500E+37	0.75603230E+13	0.78857870E+31
0.48552100E+37	0.82316740E+13	0.88379610E+31
0.51515000E+37	0.87352400E+13	0.95862580E+31
0.54477600E+37	0.92388600E+13	0.10362880E+32
0.57439900E+37	0.97425150E+13	0.11167080E+32
0.60401800E+37	0.10246220E+14	0.11998160E+32
0.65337700E+37	0.11085860E+14	0.13440860E+32
0.69285800E+37	0.11757640E+14	0.14645200E+32
0.73233400E+37	0.12429500E+14	0.15892440E+32
0.77180500E+37	0.13101440E+14	0.17181270E+32
0.82113400E+37	0.13941490E+14	0.18848650E+32
0.86059200E+37	0.14613590E+14	0.20226200E+32
0.89018100E+37	0.15117700E+14	0.21284120E+32
0.93948300E+37	0.15958020E+14	0.23093300E+32
0.98877600E+37	0.16798420E+14	0.24958070E+32

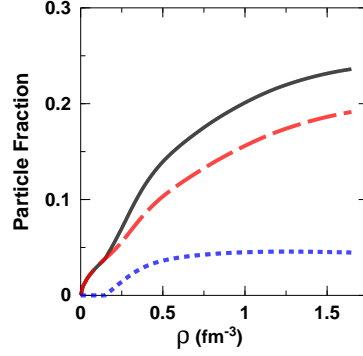


Fig. 17. (color online) Proton (solid black), electron (dashed red), and muon (dotted blue) fractions in β -stable matter as a function of total baryon density as predicted by the DBHF model.

The proton fraction in β -stable matter is calculated by imposing energy conservation and charge neutrality. The resulting algebraic equations can be found in standard literature.¹⁰³ The contribution to the energy density from the electrons is written as

$$e_e = \frac{\hbar c}{4\pi^2} (3\pi^2 \rho_e)^{4/3}, \quad (53)$$

whereas for muons we write

$$e_\mu = \rho_\mu m_\mu c^2 + (\hbar c)^2 \frac{(3\pi^2 \rho_\mu)^{5/3}}{10\pi^2 m_\mu c^2}. \quad (54)$$

These contributions are added to the baryonic part to give the total energy density. The derivative of the total energy/particle with respect to the fraction of a particular particle species is the chemical potential of that species. The conditions

$$\mu_p + \mu_e = \mu_n; \quad \mu_\mu = \mu_e; \quad \rho_p = \rho_\mu + \rho_e, \quad (55)$$

allow to solve for the densities (or fraction) of protons, electrons, and muons. Near the saturation density, when the muon fraction is close to zero, one can estimate the equilibrium proton fraction, x_p , to be⁹⁷

$$x_p \approx \left(\frac{4e_{sym}(\rho_0)}{\hbar c} \right)^3 / (3\pi^2 \rho_0). \quad (56)$$

The fractions of protons, electrons, and muons as predicted by DBHF are shown in Fig. 17. The critical density for the proton fraction to exceed approximately 1/9 and, thus, allow cooling through the direct Urca processes,

$$n \rightarrow p + e + \bar{\nu}_e \quad \text{and} \quad p + e \rightarrow n + \nu_e, \quad (57)$$

is about $0.36 - 0.39 \text{ fm}^{-3}$.

In Fig. 18, we show the mass-radius relation for a sequence of static neutron stars as predicted by the various models considered previously, see Fig. 10. ^a All models besides DBHF share the same many-body approach (BHF+TBF) but differ in the two-body potential and TBF employed. The resulting differences can be much larger than those originating from the use of different many-body approaches. This can be seen by comparing the DBHF and BOB curves, both employing the Bonn B interaction (although in the latter case the non-relativistic, r-space version of the potential is adopted). Overall, the maximum masses range from $1.8M_{\odot}$ (UIX) to $2.5M_{\odot}$ (BOB). Radii are less sensitive to the EoS and range between 10 and 12 km for all models under consideration, DBHF or BHF+TBF. Concerning consistency with present constraints, an initial observation of a neutron-star-white dwarf binary system suggested a neutron star mass (PSR J0751+1807) of $2.1 \pm 0.2M_{\odot}$.¹⁰⁵ Such observation would imply a considerable constraint on the high-density behavior of the EoS. On the other hand, a dramatically reduced value of $1.3 \pm 0.2M_{\odot}$ was reported¹⁰⁶ later, which does not invalidate any of the theoretical models under consideration.

The model dependence is shown in Fig. 19 for the case of rapidly rotating stars. The 716 Hz frequency corresponds to the most rapidly rotating pulsar, PSR J1748-2446,¹⁰⁷ although recently an X-ray burst oscillation at a frequency of 1122 Hz has been reported¹⁰⁸ which may be due to the spin rate of a neutron star. As expected, the maximum mass and the (equatorial) radius become larger with increasing rotational frequency.

Another bulk property of neutron stars is the moment of inertia, I . In Fig. 20, we show the moment of inertia at different rotational speeds (again, for all models), whereas in Fig. 21 we display the moment of inertia corresponding to the maximum mass at different rotational frequencies. These values are not in contradiction with observations of the Crab nebula luminosity. From that, a lower bound on the moment of inertia was inferred to be $I \geq 4-8 \times 10^{44} \text{ g cm}^2$, see Ref.⁹⁶ and references therein. The size of $I_{M_{max}}$ changes from model to model in line with the size of the maximum mass, see Fig. 21.

Lastly, we calculate the gravitational redshift predicted by each model. The redshift is given by

$$z = \left(1 - \frac{2M}{R}\right)^{-1/2} - 1. \quad (58)$$

This simple formula can be derived considering a photon emitted at the surface of a neutron star and moving towards a detector located at large distance.⁹⁶ The photon frequency at the emitter (receiver) is the inverse of the proper time between two wave crests in the frame of the emitter (receiver). Assuming a static gravitational field, and writing g_{00} as the metric tensor component at the surface of a nonrotating star yield the equation above. Naturally the rotation of the star modifies the

^aAll neutron star properties are calculated from public software downloaded from the website <http://www.gravity.phys.uwm.edu/rns>.

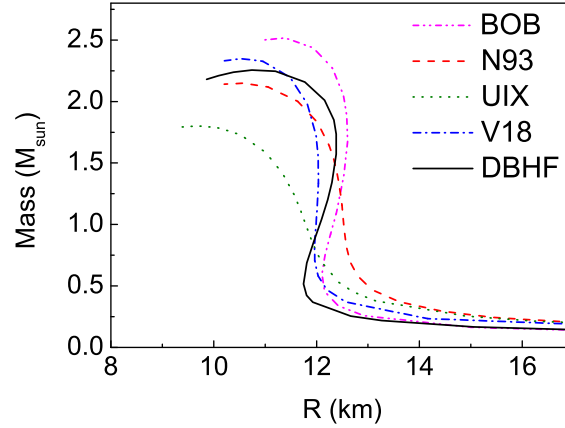


Fig. 18. (color online) Static neutron star mass-radius relation for the models considered in the text.

metric, and in that case different considerations need to be applied which result in a frequency dependence of the redshift. We will not consider the general case here.

From Fig. 22, it appears that the gravitational redshift is not very EoS-dependent (compare, for instance, the values at the maximum mass for each model), an indication that the gravitational profile at the surface of the star is similar in all models. Thus measurements of z may not be the best way to discriminate among different EoS.

Clearly, at the densities probed by the interior of neutron stars the model dependence is large, but presently available constraints are still insufficient to discriminate among these EoS. At very high density (ρ between five and ten times normal density), the most repulsive *symmetric matter* energies are produced with BOB, V18, DBHF, N93 and UIX, in that order. This explains the maximum mass predictions, which depend mostly on the absolute repulsion present in the symmetric matter EoS. In pure neutron matter, N93 follows right after BOB (again, from largest to smallest repulsion). This indicates a somewhat different balance of attraction/repulsion when only $T=1$ contributions are included. The symmetry energy, see Fig. 10, which depends entirely on the repulsion of neutron matter *relative* to symmetric matter and whose density dependence controls observables such as the neutron skin, is largest in N93, followed by BOB, V18, UIX, and DBHF.

The model dependence we observe comes from two sources, the two-body potential and the many-body approach, specifically the presence of explicit TBF or Dirac effects. The dependence on the two-body potential is very large. Typically, the main source of model dependence among NN potentials is found in the strength of the tensor force. Of course, differences at the two-body level impact the TBF as

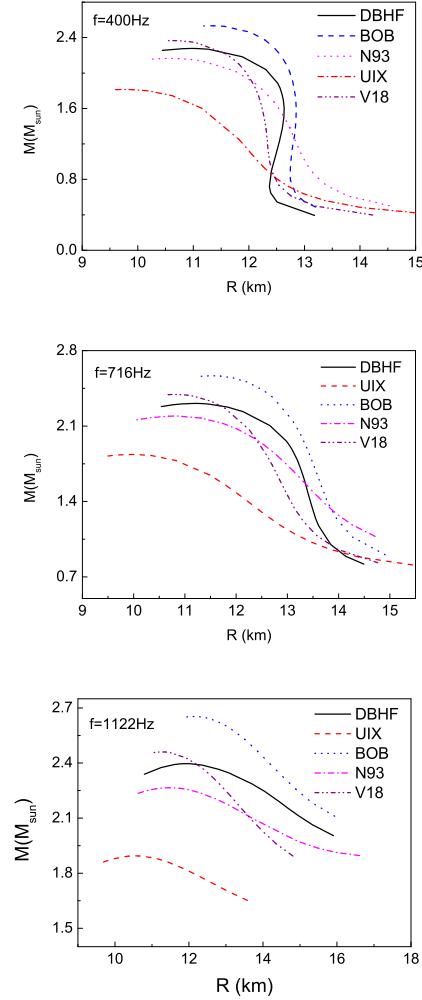


Fig. 19. (color online) Mass-radius relation for the models considered in the text and for different rotational frequencies.

well, whether they are microscopic or phenomenological (as in the case of UIX).

On the other hand, when comparing DBHF and BOB, we are looking at differences stemming from the many-body scheme, as the two models share the same NN potential. In the BOB model, repulsion grows at a much faster rate than in DBHF, and more strongly so in neutron matter. (Hence, the much larger symmetry energy with BOB). As an example, at about 6 times normal density the DBHF energy of symmetric matter is 67% of the BOB energy and only 51% at ten times normal densities. In pure neutron matter, those ratios become 49% and 30%, respectively.

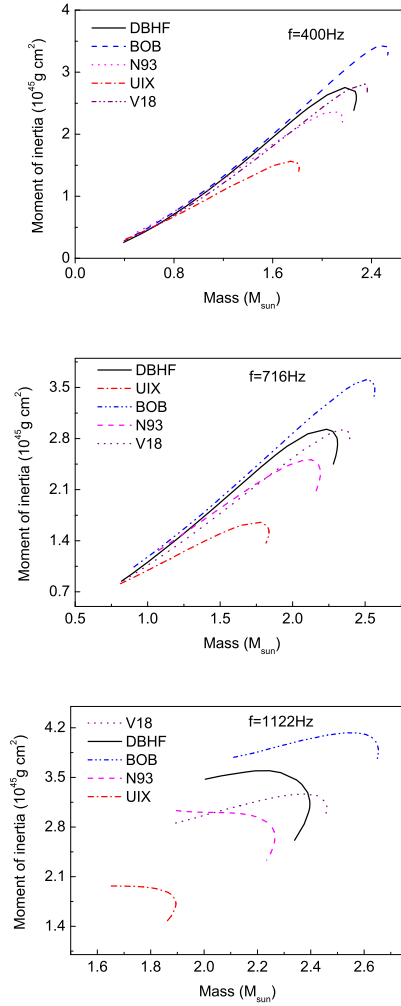


Fig. 20. (color online) Moment of inertia for the models considered in the text and for different rotational frequencies.

Thus, the inclusion of the microscopic TBF in the BHF model introduces considerable more repulsion than the Dirac effects through highly non-linear terms.⁴⁹ Both attractive and repulsive TBF are required for a realistic description of the saturation point. The density dependence of the repulsive terms is obviously stronger and thus dominates at high density. Furthermore, it appears that this is especially true in neutron matter.

In Ref.⁴⁹ it is shown that the largest contribution to the net TBF originates from Z-diagrams such as shown in Fig. 2, a fact which confirms the validity of the

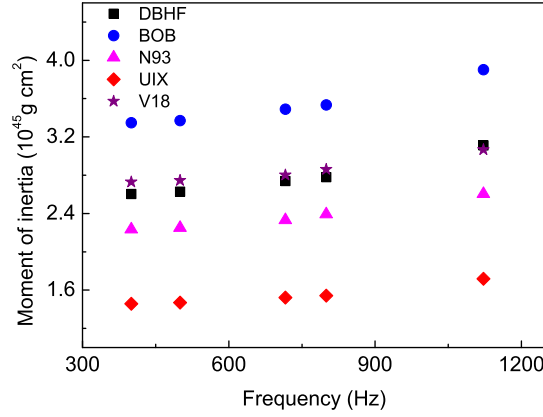


Fig. 21. (color online) Moment of inertia corresponding to the maximum mass for the models considered in the text as a function of the rotational frequency.

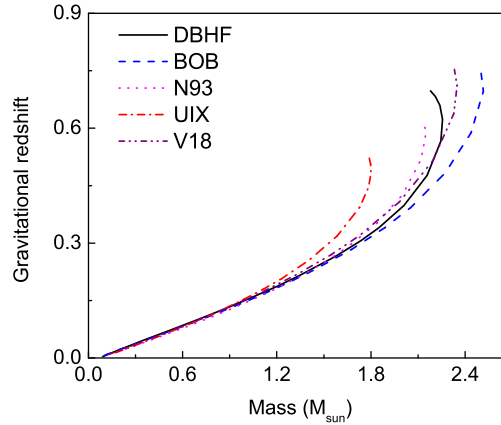


Fig. 22. (color online) Gravitational redshift for all models. For each model, the corresponding sequence of static stars is considered.

DBHF approximation. The actual amount of repulsion, however, seems to depend sensitively upon the TBF parametrization. One of the advantages of the DBHF method is the ability to avoid possible inconsistencies between the parameters of the two- and the three-body systems.

At this time, available constraints cannot pin down the high-density behavior of the EoS. Nevertheless, we argue again that microscopic models allow for a deeper insight into the origin of the observed physical effects, and should be pursued along with improved constraints.

5. Non-Nucleonic Degrees of Freedom

5.1. Introduction

At densities close to normal nuclear density, protons and neutrons are the only baryonic degrees of freedom. As density increases, other baryons begin to appear, such as strange baryons or isospin 3/2 nucleon resonances. Hyperonic states can be classified according to the irreducible representation of the $SU(3)$ group. The octet of baryons that can appear in neutron matter includes nucleons, Λ , $\Sigma^{0,\pm}$, and $\Xi^{0,-}$.

Neglecting the nucleon-hyperon interaction, the threshold for stable hyperons to exist in matter is determined by comparing the hyperon mass with the neutron Fermi energy, which is the largest available energy scale in neutron-rich matter. We consider cold neutron stars, after neutrinos have escaped. Strange baryons appear at about 2-3 times normal density,¹⁰⁹ an estimate which is essentially model independent, through the processes $n+n \rightarrow p+\Sigma^-$ and $n+n \rightarrow n+\Lambda$. The equilibrium conditions for these reactions are

$$2\mu_n = \mu_p + \mu_{\Sigma^-} ; \mu_n = \mu_{\Lambda} . \quad (59)$$

Also, we have

$$\mu_e = \mu_{\mu} ; \mu_n = \mu_p + \mu_e , \quad (60)$$

the equations above being special cases of

$$\mu = b\mu_n - q\mu_e , \quad (61)$$

where b and q are the baryon number and the charge (in units of the electron charge) of the particular species with chemical potential μ . Together with the charge neutrality condition and baryon number conservation,

$$\rho_p = \rho_e + \rho_{\mu} + \rho_{\Sigma^-} ; \rho = \rho_n + \rho_p + \rho_{\Sigma^-} + \rho_{\Lambda} , \quad (62)$$

the above system allows to determine the various particle fractions.

Clearly, the composition of matter at supra-nuclear densities determines the behavior of stellar matter. It is also speculated that a transition to a quark phase may take place at very high densities, the occurrence of which depends sensitively on the properties of the EoS in the hadronic (confined) phase. The presence of hyperons in the interior of neutron stars is reported to soften the equation of state, with the consequence that the predicted neutron star maximum masses become considerably smaller.¹¹⁰ With recent constraints allowing maximum masses larger than previously accepted limits (see previous section), accurate microscopic calculations which include strangeness (in addition to other important effects, such as those originating from relativity), become especially timely.

Thus, there are strong motivations for including strange baryons in nuclear matter. Moreover, as far as terrestrial nuclear physics is concerned, studies of hyperon energies in nuclear matter naturally complement our knowledge of hypernuclei (see, for instance, Refs.^{111,112,113,114}). For example, the EoS of hypermatter is useful

in the development of generalized mass formulas depending on both density and hyperon fraction.^{114,115} From the experimental side, additional data are very much needed, especially on $\Lambda\Lambda$ hypernuclei, which would provide information on the Λ – Λ interaction. Concerning single hypernuclei, analyses of data on Λ binding energies constrain the depth of the single- Λ potential to be 27–30 MeV.¹¹⁶ The status of Σ hypernuclei and the Σ -nucleus potential is more controversial (see Ref.¹¹⁷ and references therein).

5.2. Hyperons and neutron star matter

Interacting hypernuclear matter was initially studied within variational approaches.^{118,119} Relativistic mean field models were also extended to include hyperons.^{120,121,122,123} Microscopic models require inclusion of realistic nucleon-hyperon and hyperon-hyperon interactions,^{124,125,126,127} but the experimental information on these interactions is still scarce. The nucleon-hyperon potentials are fitted to ΛN or ΣN scattering data. The information on the hyperon-hyperon interaction is limited to the ground state of double- Λ hypernuclei.¹²⁸ Additional constraints can be derived from $SU(3)$ symmetry arguments.

The common denominator among microscopic calculations of the EoS with hyperons is that they are typically conducted within a non-relativistic framework together with r -space local nucleon-hyperon (NY) potentials. Microscopic calculations of nuclear matter properties including hyperons have been reported earlier within the non-relativistic Brueckner-Hartree-Fock framework (BHF) (see, for instance, Refs.^{109,115}), using the Nijmegen¹²⁵ nucleon-hyperon (NY) meson-exchange potential. Extensive microscopic work on hyperonic nuclear matter, again within the non-relativistic BHF framework, has also been published by the Barcelona group (see, for instance, Refs.^{129,130,131,132}).

The issue of interacting hyperons and their impact on the β -stable EoS and neutron star structure has been confronted, for instance, in Ref.¹³³ using the Paris¹³⁴ and the Argonne V18⁶⁴ NN potentials together with the Nijmegen soft-core (NSC89) NY potential.¹²⁵ A remarkable conclusion from that work is that, in the presence of hyperons, the inclusion of nucleonic TBF does not alter the EoS appreciably. With nucleons only, TBF bring in considerable repulsion at high density which result in a much stiffer EoS. On the other hand, when hyperons are present the nucleonic TBF increase the strange baryon population due to the increased nucleon chemical potential. In turn, this decreases the nucleon population with the final net effect on the EoS found to be very small. In other words, it would be necessary for the NY interaction to become very repulsive at high density to compensate for the loss of nucleons and gain a substantial increase of the star maximum mass.¹³³ Results for the neutron star maximum gravitational mass, radius, and central density are shown in Table 6. The use of different NN potentials seem to produce only small variations.

More recently, neutron star structure results have been revisited by the Catania

Table 6. Neutron star limiting values for different EoS with (Y) and without (no Y) hyperons as from Ref.¹³².

EoS	M_{max}/M_{\odot}		$R(km)$		$\rho_c(fm^{-3})$	
	no Y	Y	no Y	Y	no Y	Y
V18	1.64	1.26	9.10	8.70	1.53	1.86
Paris	1.67	1.31	8.90	8.62	1.59	1.84
V18+TBF	2.00	1.22	10.54	10.46	1.11	1.25
Paris+TBF	2.06	1.26	10.50	10.46	1.10	1.25

group with the microscopic models we considered earlier in this article (BHF+TBF models from Ref.⁶³) along with the NSC89 nucleon-hyperon interaction.¹²⁵ There, the nucleonic energy densities obtained with the different NN interactions are used together with the same NY interaction to calculate stellar matter. It is found that the inclusion of hyperons reduces dramatically the maximum mass. It also reduces substantially the maximum mass range covered by the models, which goes from 1.8 to 2.5 M_{\odot} with nucleonic energy densities only, see Fig. 18, to the much narrower intervals of 1.3-1.4 M_{\odot} . Furthermore, the stiffer the original EoS, the larger the softening effect from the presence of strangeness. Thus, in this approach, one may conclude that hybrid stars (containing hadronic and quark matter) are necessary to reproduce the larger mass values consistent with recent observations.

Overall, there seems to be a consensus among microscopic calculations of the BHF type (with or without TBF) that the inclusion of hyperons yields a remarkably low value of a neutron star maximum mass. On the other hand, predictions from different versions of relativistic mean field models are quite different from one another.^{135,136}

The alternative approach to the EoS with strange baryons presented in the next section will suggest that present NY interactions are not yet sufficiently constrained to allow for definite conclusions concerning the occurrence of a hybrid phase.

5.3. A first DBHF calculation of the EoS with nucleons and Λ -hyperons

It is one purpose of this section to bring in the new aspect of Dirac effects on the Λ hyperon as well as the nucleon. By “Dirac effects” we mean that the single-baryon wavefunction is calculated self-consistently with the appropriate effective interaction. The origin and nature of these effects on the nucleonic equation of state was discussed previously, see Sec. 3.2.1.

A previous calculation from the Idaho group¹³⁷ of the binding energy of a Λ impurity in nuclear matter showed that Dirac effects on the Λ hyperon yield a moderate reduction of the binding energy. In that calculation, we used the most

recent nucleon-hyperon (NY) potential reported in Ref.¹³⁸ (thereafter referred to as NY05), and observed that G -matrix predictions obtained with NY05 are significantly different from calculations using the previous (energy independent) version of the Jülich NY potential¹³⁹. Therefore, in this work we will use both potentials, for comparison. As usual, the Bonn B potential¹ is used throughout for the nucleon-nucleon (NN) part.

Previous calculations of the EoS with hyperons have typically been conducted within a non-relativistic framework together with r -space local NY potentials. The DBHF calculation we describe here uses non-local relativistic momentum-space (NN and NY) potentials and a relativistic many-body method, and is therefore fundamentally different. Next we give a brief review of the formalism.

The single-nucleon and single- Λ potentials are obtained as

$$U_N(\vec{k}_N) = U_{N\Lambda}(\vec{k}_N) + U_{NN}(\vec{k}_N), \quad (63)$$

and

$$U_\Lambda(\vec{k}_\Lambda) = U_{\Lambda N}(\vec{k}_\Lambda), \quad (64)$$

i.e., the $\Lambda\Lambda$ interaction is neglected. In the equations above, the various terms, $U_{B_1 B_2}$, are the contributions to the potential of baryon B_1 from its interaction with all baryons of type B_2 . They are given by

$$U_{N\Lambda}(\vec{k}_N) = \sum_{T,L,S,J} \frac{(2T+1)(2J+1)}{(2t_N+1)(2s_N+1)} \int_0^{k_F^\Lambda} G_{N\Lambda}^{T,L,S,J}(k(\vec{k}_N, \vec{k}_\Lambda), P(\vec{k}_N, \vec{k}_\Lambda)) d^3 k_\Lambda, \quad (65)$$

$$U_{NN}(\vec{k}_N) = \sum_{T,L,S,J} \frac{(2T+1)(2J+1)}{(2t_N+1)(2s_N+1)} \int_0^{k_F^N} G_{NN}^{T,L,S,J}(k(\vec{k}_N, \vec{k}'_N), P(\vec{k}_N, \vec{k}'_N)) d^3 k'_N, \quad (66)$$

and

$$U_{\Lambda N}(\vec{k}_\Lambda) = \sum_{T,L,S,J} \frac{(2T+1)(2J+1)}{(2t_\Lambda+1)(2s_\Lambda+1)} \int_0^{k_F^N} G_{\Lambda N}^{T,L,S,J}(k(\vec{k}_N, \vec{k}_\Lambda), P(\vec{k}_N, \vec{k}_\Lambda)) d^3 k_N, \quad (67)$$

where the channel isospin T can be 0 or 1 for the NN case and is equal to 1/2 for the $N\Lambda$ case, and s_i, t_i ($i = N, \Lambda$) are the spin and isospin of the nucleon or Λ .

Notice that

$$\frac{U_{N\Lambda}}{U_{\Lambda N}} \approx \frac{\rho_\Lambda}{\rho_N}, \quad (68)$$

an approximation often used in mean-field approaches.

The average potential energies of nucleons and Λ 's are determined from

$$\langle U_N \rangle = \frac{1}{\rho_N} \frac{1}{(2\pi)^3} 4 \frac{1}{2} \int_0^{k_F^N} U_N(\vec{k}_N) dk_N^3, \quad (69)$$

and

$$\langle U_\Lambda \rangle = \frac{1}{\rho_\Lambda} \frac{1}{(2\pi)^3} 2 \frac{1}{2} \int_0^{k_F^\Lambda} U_\Lambda(\vec{k}_\Lambda) dk_\Lambda^3, \quad (70)$$

where the factors of 4 and 2 in Eqs. (69) and Eq. (70), respectively, account for protons and neutrons in both spin states or Λ 's in both spin states.

Finally the average potential energy per baryon is obtained as

$$\langle U \rangle = \frac{\rho_N \langle U_N \rangle + \rho_\Lambda \langle U_\Lambda \rangle}{\rho_{tot}}, \quad (71)$$

from which, together with a similar expression for the kinetic energy, one obtains the average energy per baryon.

The NA G -matrix is obtained from the Bethe-Goldstone equation

$$\begin{aligned} \langle N\Lambda | G_{N\Lambda}(E_0) | N\Lambda \rangle &= \langle N\Lambda | V | N\Lambda \rangle \\ &+ \sum_{Y=\Lambda, \Sigma} \langle N\Lambda | V | NY \rangle \frac{Q}{E_0 - E} \langle NY | G_{N\Lambda}(E_0) | N\Lambda \rangle, \end{aligned} \quad (72)$$

where E_0 and E are the starting energy and the energy of the intermediate NY state, respectively, and V is an energy-independent NY potential.

For two particles with masses M_N and M_Λ and Fermi momenta k_F^N and k_F^Λ , Pauli blocking requires

$$Q(\vec{k}, \vec{P}) = \begin{cases} 1 & |\beta\vec{P} + \vec{k}| > k_F^\Lambda \text{ and } |\alpha\vec{P} - \vec{k}| > k_F^N \\ 0 & \text{otherwise.} \end{cases} \quad (73)$$

The above condition implies the restriction

$$\frac{(\frac{M_N}{M}P)^2 + k^2 - (k_F^N)^2}{2Pk \frac{M_N}{M}} > \cos\theta > -\frac{(\frac{M_\Lambda}{M}P)^2 + k^2 - (k_F^\Lambda)^2}{2Pk \frac{M_\Lambda}{M}}, \quad (74)$$

where θ is the angle between the total (\vec{P}) and the relative (\vec{k}) momenta of the two particles, and $M = M_\Lambda + M_N$. Angle-averaging is then applied in the usual way.

In the present calculation we consider a non-vanishing density of Λ 's but do not allow for the presence of real Σ 's in the medium (although both Λ and Σ are included in the coupled-channel calculation of the NY G -matrix, see Eq. (73)). Essentially we are considering a scenario where a small fraction of nucleons is replaced with Λ 's, as could be accomplished by an experiment aimed at producing multi- Λ hypernuclei. Multistrange systems, such as those produced in heavy-ion collisions, may of course contain other hyperons on the outset. For small Λ densities, though, as those we consider here, the cascade (Ξ) and the Σ hyperon are expected to decay quickly through the strong processes $N + \Xi \rightarrow \Lambda + \Lambda$ and $N + \Sigma \rightarrow N + \Lambda$. Under these conditions, a mixture of nucleons and Λ 's can be considered "metastable", in the sense of being equilibrated over a time scale which is long relative to strong processes. (In fact, the strong reactions mentioned above would have to be Pauli blocked in order to produce a metastable multistrange system¹⁴⁰.)

We neglect the YY' interaction, as very little is known about it. Furthermore, non-local momentum-space YY potentials, appropriate for our DBHF framework, are not available at this time. For these reasons, we keep the Λ concentration relatively low.

We have incorporated DBHF effects in the Λ matter calculation, which amounts to involving the Λ single-particle Dirac wave function in the self-consistent calculation through the Λ effective mass, M_Λ^* .¹⁴¹ However, a problem that needs to be addressed with the Jülich NY potential in conjunction with DBHF calculations is the use of the pseudoscalar coupling for the interactions of pseudoscalar mesons (pions and kaons) with nucleons and hyperons. For the reasons described in Sec. 3.2.1 (that is, the close relationship between Dirac effects and “Z-diagram” contributions), this relativistic correction is known to become unreasonably large when applied to a vertex involving pseudoscalar coupling. On the other hand, the gradient (pseudovector) coupling (also supported by chiral symmetry arguments) largely suppresses antiparticle contributions. To resolve this problem, one can make use of the on-shell equivalence between the pseudoscalar and the pseudovector coupling, which amounts to relating the coupling constants as follows:

$$g_{ps} = f_{pv} \frac{M_i + M_j}{m_{ps}}, \quad (75)$$

where g_{ps} denotes the pseudoscalar coupling constant and f_{pv} the pseudovector one; m_{ps} , M_i , and M_j are the masses of the pseudoscalar meson and the two baryons involved in the vertex, respectively. This procedure can be made plausible by writing down the appropriate one-boson-exchange amplitudes and observing that, redefining the coupling constants as above, we have (see Ref.¹ for the two-nucleon case)

$$V_{pv} = V_{ps} + \dots \quad (76)$$

where the ellipsis stands for off-shell contributions. Thus, the pseudoscalar coupling can be interpreted as pseudovector coupling where the off-shell terms are ignored. This is what we apply in our DBHF calculations. More concretely, from a given pseudoscalar potential, first we extract the corresponding f_{pv} from Eq. (75). In the medium, V_{ps}^* will contain the coupling constant $g = \frac{M_i + M_j}{m_{ps}} f_{pv}$. When the baryon masses are reduced through the effective mass prescription, the reduction of the masses appearing at the denominator of the momentum-dependent part of the potential will be “balanced” by the equally reduced masses at the numerator of the coupling constant. This prescription prevents the OBE diagram from growing to unreasonably large values when effective masses are employed.

Next, we will be showing results for both the NY05 potential¹³⁸ and the previous version of the Jülich NY potential, NY94, specifically the model referred to as \tilde{A} in Ref.¹³⁹.

In Fig. 23 we show the energy per particle as a function of density for different Λ concentrations as obtained from DBHF calculations along with the NY94 potential.

As more nucleons are replaced with Λ 's, generally less binding energy per particle is generated. This is due to the weaker nature of the $N\Lambda$ interaction relative to the NN one. Furthermore, the Λ Fermi momentum grows rather quickly with ρ_Λ , since only two Λ 's can occupy each state, rather than four, which implies a fast rise of the hyperon kinetic energy. (Although, for small hyperon densities, there is at first some reduction of the kinetic energy, due to the fact that Λ 's have larger mass and can occupy lower energy levels.) We notice that the saturation density remains essentially unchanged with increasing hyperon concentrations. As density grows, though, larger Λ concentrations start to yield increased attraction. One must keep in mind that, especially at the higher densities, the NN interaction become less and less attractive due to medium effects, in particular repulsive Dirac effects. Thus, removing nucleons from the system can actually amount to increased binding.

Moving now to Fig. 24, where the NY05 potential is adopted, we see a very different scenario. We recall that the NY05 model is considerably more attractive, yielding about 50 MeV for the Λ binding energy^{137,142} whereas a value close to 30 MeV was found with NY94¹³⁹. Naturally, we expect these differences to reflect onto the respective EoS predictions. Here, increasing the hyperon population yields more binding, a trend opposite to the one seen in the previous figure. Again, the final balance is the result of a combination of effects. The fact that the NN component is repulsive at the higher densities, together with the more attractive nature of the NY05 potential, determines here a net increase in attraction with decreasing *nucleon* density. However, the additional binding becomes smaller and smaller with increasing hyperon concentration, indicating that, at sufficiently large Λ densities, the net balance may turn repulsive. Notice also that in Fig. 24 the minimum moves towards higher densities, signifying that baryon pairs favor a smaller interparticle distance.

To summarize, one must keep in mind that the energy/particle is the result of a delicate balance of both the kinetic energies and the potential energies of the two baryon species, being weighed by the respective densities. Thus, although the NN interaction is generally more attractive than the $N\Lambda$ one, the net effect of replacing nucleons with Λ 's will depend sensitively on the nature of the NY interaction that's being put into the system, as well as the "stiffness" of the original, nucleonic, EoS.

This is further confirmed in Fig. 25, where we show predictions from conventional BHF calculations (i.e., no "Dirac" effects). As in the previous figures, the red curve is the nucleonic EoS. The solid(dashed) curves are the predictions with NY94(NY05). Clearly, the effects are opposite depending on the NY interaction. Qualitatively, the trend seen in each group of curves (solid or dash) is approximately consistent with the one observed previously in the corresponding (i. e. same NY potential) DBHF predictions. However, the "cross over" of the curves seen in Fig. 23 at about twice saturation density is due to a large extent to the more repulsive nature of the nucleonic EoS in the DBHF calculation (see comments above).

In conclusion, the effect of hyperons on the EoS is strongly dependent upon the baseline (nucleonic) EoS as well as the NY potential model. With regard to the

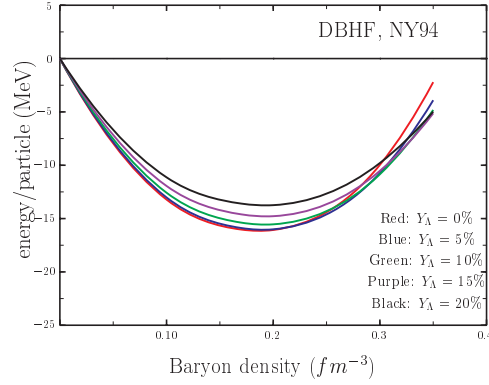


Fig. 23. (Color online) Energy/particle as a function of density in symmetric nuclear matter for various Λ concentrations Y_Λ . Predictions obtained from DBHF calculations with the NY94 potential.

first issue, we stress the importance of starting from a realistic EoS, such as the one predicted in DBHF calculations or obtained with the inclusion of three-body forces. The second observation confirms the conclusions of Ref.¹⁴³ concerning the large uncertainties originating from the bare NY potentials. Unfortunately, the existing data do not set sufficient constraints on the potentials, as demonstrated by the fact that different potentials can fit the available scattering data equally accurately but produce very different scattering lengths¹⁴³.

Of course, the actual fraction of hyperons present in star matter must be determined by the equations of β stability and charge neutrality for highly asymmetric matter containing neutrons, protons, hyperons, and leptons as described in Sec. 5.1. What we have learnt at this time is that the predicted energy/particle in symmetric matter is very sensitive to the chosen NY interaction. The uncertainties due to the model dependence discussed in this paper are likely to impact any conclusions on the properties of strange neutron stars, which therefore must be interpreted with caution. These include considerations of deconfinement and possible transition from hadronic to quark matter, which depend sensitively on the equation of state in the hadronic phase.

5.4. Neutron star matter with non-interacting hyperons

As anticipated at the end of Sec. 5.2, the uncertainties that we have demonstrated in Sec. 5.3 suggest that present NY interactions are not sufficiently constrained to allow for robust conclusions concerning the occurrence of a hybrid phase. Therefore, to

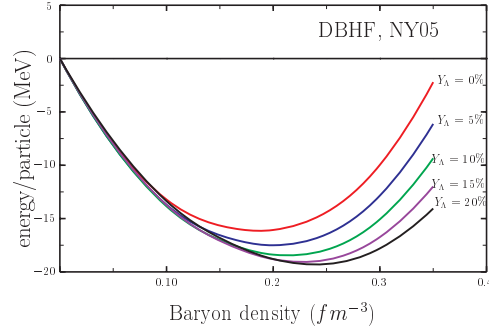


Fig. 24. (Color online) Energy/particle as a function of density in symmetric nuclear matter for various Λ concentrations Y_Λ . Predictions obtained from DBHF calculations with the NY05 potential.

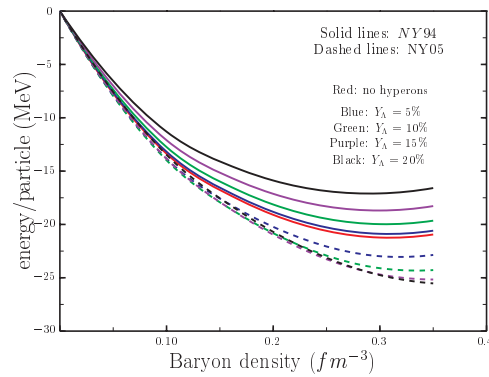


Fig. 25. (Color online) Energy/particle as a function of density in symmetric nuclear matter for various Λ concentrations. Predictions obtained from BHF calculations. The solid(dashed) lines are obtained with the NY94(NY05) potentials.

avoid those uncertainties, we will now try to *estimate* the impact of hyperons on the β -stable DBHF EoS considering *non-interacting* hyperons. Equations (59,60,62) are solved (for fixed total baryon density) treating Λ and Σ^- as free (non-relativistic) fermions. The nucleonic energies are taken from our DBHF EoS for IANM, eval-

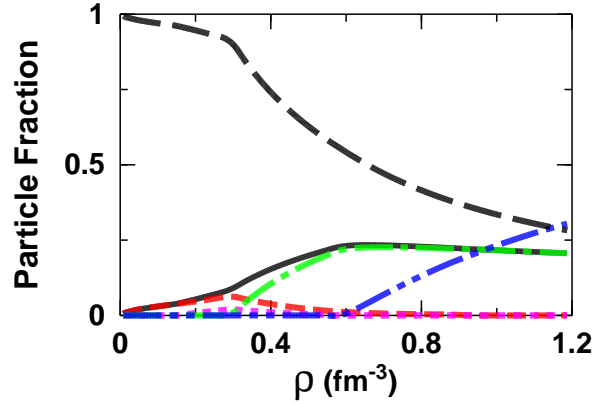


Fig. 26. (color online) Various particle fractions in β -stable matter. Neutron: long-dashed black; proton: solid black; Σ^- : dash-dotted green; Λ : dash-double-dotted blue; electrons: short-dashed red; muons: dotted purple.

uated at some nucleon density, $\rho_n + \rho_p$, with ρ_n and ρ_p to be determined along with the other particle fractions. (To allow for the solution of the 6×6 (including the normalization condition) system of algebraic equations for the six unknown particle concentrations, our nucleonic EoS is first parametrized in terms of analytic functions of density.) Those fractions are shown in Fig. 26. The trend is very similar to the one shown in Ref.¹³³ with free hyperons, which, in turn, is qualitatively consistent with the one seen when the NY interaction is turned on.¹³³ The onset of the Σ^- baryon occurs at a density of about 0.3 fm^{-3} . Leptons start to disappear from the system after hyperon formation, an indication that charge neutrality through Σ^- production is energetically more favorable than through β decay. The onset of Λ production occurs at a density of approximately 0.6 fm^{-3} . These thresholds are in good agreement with those reported in Ref.¹³³ for both free and interacting hyperons, when the BHF+TBF predictions are considered (the TBF shifts down the threshold densities for Λ and Σ^- formation as compared with the case of two-body forces only).

In Fig. 27, we show the pressure in β -stable matter with the Idaho DBHF EoS with and without (free) hyperons. The differences are dramatic but consistent with previous observations.¹³³ The effect of including the NY interaction is quite small compared with the differences seen in Fig. 27. Thus, one conclusion seems appropriate at this point: Regardless the chosen NY interaction, the effect of adding strange baryons is a dramatic softening of the EoS, (consistent with a large reduction of the neutron star maximum mass). *Furthermore, given the uncertainties*

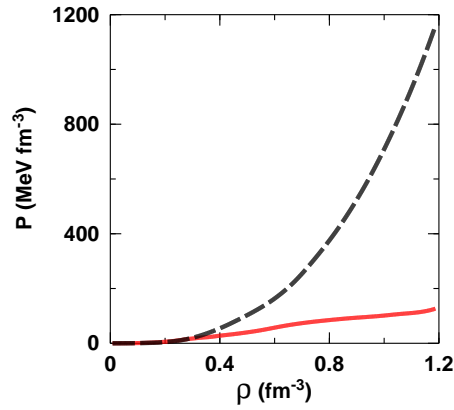


Fig. 27. (color online) Pressure in β -stable matter from the DBHF calculation with no hyperons (black dash) and with free hyperons (solid red).

arising from the NY potential demonstrated in the previous section, the effect of free hyperons may very well provide a realistic, average estimate of the impact of including strangeness.

In Fig. 28 we compare energy densities in β -stable matter as obtained from the Idaho DBHF EoS with free hyperons and from the two models (AV18 + TBF, Paris + TBF) used in Ref.¹³³ along with the NSC NY potential.¹²⁵ The similarity between the curves indicates that the effect of including the NY interaction in star matter is relatively small and/or that differences in the respective nucleonic EoS may compensate those which originate from the treatment of hyperons.

The neutron star maximum mass we obtain with the DBHF EoS and free hyperons is close to $1.2 M_{\odot}$. Considering that inclusion of the NY interaction would increase the pressure at high density, this result is not inconsistent with those shown in Table 6. In summary, our analysis confirms a large softening of the β -stable EoS as a consequence of including strange baryons, accompanied by a strong reduction of the maximum mass, a conclusion that appears to be nearly model independent. The softening is mostly caused by conversion of the kinetic energy of the existing particle species into masses of the newly produced particles. The resulting maximum mass reduction appears in contradiction with present constraints, and thus leaves intriguing questions open concerning phase transitions and degrees of freedom appropriate for high-density stellar matter.

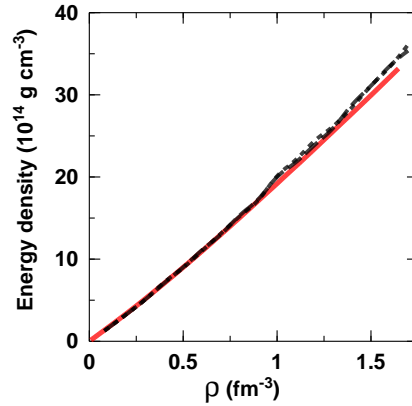


Fig. 28. (color online) Energy density in β -stable matter from various models: The black dashed and dotted lines (essentially identical) are the results of BHF calculations with the Argonne V18 and the Paris potentials, respectively, including TBF and hyperons interacting via the Nijmegen soft-core NY potential (see Ref.¹³²). The red solid line is obtained with the DBHF calculation for the nucleonic EoS and free hyperons.

6. Conclusions and Outlook

The EoS of hadronic matter enters in a variety of systems, from atomic nuclei to the most compact form of matter found in the universe, namely the matter in the interior of neutron stars. EoS-related properties can and should be calculated *ab initio* and consistently from the same basic nuclear forces. They include: the nuclear matter “optical potential”, effective in-medium cross sections, nucleon mean free path in nuclear matter, neutron skins, and neutron star properties.

We have reviewed recent calculations of the EoS, over a large range of densities and isospin asymmetries, with a particular eye on the microscopic approach. The obvious advantage of the latter lies in the opportunity of interpreting the predictions in terms of the input nuclear forces and their behavior in the many-body environment. In turn, this facilitates the identification of potentially missing dynamics.

We have discussed differences among microscopic models which do or do not include explicit TBF. It is quite clear that model dependence amongst predictions can be quite large. Naturally, this is especially the case at those densities where constraints are the weakest.

Rich and diverse effort is presently going on to improve the available constraints on the EoS or find new ones. These constraints are usually extracted through the

analysis of selected heavy-ion collision observables. At the same time, partnership between nuclear physics and astrophysics is becoming increasingly important towards advancing our understanding of exotic matter. Perhaps the best prospects to discriminate among families of EoS, especially at high density, are in more accurate measurements of neutron stars radii and/or moments of inertia.

Other EoS-related issues of contemporary interest which we have not reviewed here include temperature dependence and polarizability of nuclear/neutron matter. Knowledge of the finite-temperature EoS plays a crucial role in the final stages of a supernova evolution. Microscopic models which can successfully describe the ground state of nuclear matter should be the starting point to move on to its excited states.

As a final note, the emergence of FRIB¹⁸ will mark a turning point in the progress of experimental nuclear physics, possibly unveiling unknown areas on the nuclear chart. It is thus imperative that such large-scale projects be constantly supported by theoretical calculations with predictive power.

Acknowledgements

Support from the U.S. Department of Energy under grant DE-FG02-03ER41270 is gratefully acknowledged. I like to thank D. Alonso and P. Liu for their help in various phases of the Idaho project. I am grateful to M. Baldo, U. Lombardo, and H.-J. Schulze for useful communications, to F. Weber for providing the crustal EoS, and to J. Heidenbauer for providing the nucleon-hyperon potential code.

References

1. R. Machleidt, *Adv. Nucl. Phys.* **19** (1989) 189.
2. K. Oyamatsu, I. Tanihata, Y. Sugahara, K. Sumiyoshi, and H. Toki, *Nucl. Phys.* **A634** (1998) 3.
3. R.J. Furnstahl, *Nucl. Phys.* **A706** (2002) 85.
4. F. Sammarruca and Pei Liu, *Phys. Rev. C* **79** (2009) 057301.
5. K.A. Brueckner, C.A. Levinson, and H.M. Mahmoud, *Phys. Rev.* **95** (1954) 217.
6. H.A. Bethe, *Phys. Rev.* **103** (1956) 1353.
7. J. Goldstone, *Proc. R. Soc. London, Ser. A* **239** (1957) 267.
8. H.A. Bethe, *Annu. Rev. Nucl. Sci.* **21** (1971) 93.
9. M.I. Haftel and F. Tabakin, *Nucl. Phys.* **A158** (1970) 1.
10. D.W.L. Sprung, *Adv. Nucl. Phys.* **5** (1972) 225.
11. V.R. Pandharipande and R.B. Wiringa, *Rev. Mod. Phys.* **51** (1979) 821.
12. I.E. Lagaris and V.R. Pandharipande, *Nucl. Phys.* **A359** (1981) 349.
13. B.D. Day and R.B. Wiringa, *Phys. Rev. C* **32** (1985) 1057.
14. M.R. Anastasio, L.S. Celenza, W.S. Pong, and C.M. Shakin, *Phys. Rep.* **100** (1983) 327.
15. C.J. Horowitz and B.D. Serot, *Phys. Lett.* **137B** (1984) 287; *Nucl. Phys.* **A464** (1987) 613.
16. R. Brockmann and R. Machleidt, *Phys. Lett.* **149B** (1984) 283; *Phys. Rev. C* **42** (1990) 1965.
17. S. Weinberg, *Physica* **96A** (1979) 327; *Phys. Lett.* **B251** (1990) 288.

18. <http://www.frib.msu.edu/>
19. K.A. Brueckner and S.A. Coon, *Phys. Rev.* **168** (1968) 1184.
20. P.J. Siemens, *Nucl. Phys.* **A141** (1970) 225.
21. M. Beiner, H. Flocard, Nguyen Van Giai, and P. Quentin, *Nucl. Phys.* **A238** (1975) 29.
22. Y. Sugahara and H. Toki, *Nucl. Phys.* **A579** (1994) 557.
23. A. Akmal, V.R. Pandharipande, and D.G. Ravenhall, *Phys. Rev. C* **58** (1998) 1804.
24. C. Fuchs, H. Lenske, and H.H. Wolter, *Phys. Rev. C* **52** (1995) 3043.
25. F. Hofmann, C.M. Keil, and H. Lenske, *Phys. Rev. C* **64** (2001) 034314.
26. I. Bombaci and U. Lombardo, *Phys. Rev. C* **44** (1991) 1892.
27. W. Zuo, I. Bombaci, and U. Lombardo, *Phys. Rev. C* **60** (1999) 024605.
28. L. Engvik, M. Hjorth-Jensen, and E. Osnes, *Phys. Rev. Lett.* **73** (1994) 2650; L. Engvik, E. Osnes, M. Hjorth-Jensen, G. Bao, and E. Østgaard, *Astrophysical J.* **469** (1996) 794.
29. D. Alonso and F. Sammarruca, *Phys. Rev. C* **67** (2003) 054301.
30. E.N.E. van Dalen, C. Fuchs, and A. Faessler, *Nucl. Phys.* **A74** (2004) 227; *Phys. Rev. C* **72** (2005) 065803.
31. Andrew W. Steiner, *Phys. Rev. C* **74** (2006) 045808, and references therein.
32. W. Trautmann *et al.*, arXiv:0907.2822 [nucl-ex]; C. Sfienti *et al.*, *Phys. Rev. Lett.* **102** (2009) 152701.
33. M.B. Tsang *et al.* *Phys. Rev. Lett.* **102** (2009) 12701.
34. V. Greco, arXiv:08122806 [nucl-th]; Proceedings of the “International Workshop on Nuclear Dynamics in Heavy-Ion Reactions and the Symmetry Energy (IWND2009)”, Shanghai, China, August 23-25, 2009, to be published.
35. B. Borderie and M.F. Rivet, *Prog. Part. Nucl. Phys.* **61** (2008) 551; arXiv:0812.3524 [nucl-ex].
36. Gao-Chan Yong, arXiv:0906.0939 [nucl-th]; Proceedings of the “International Workshop on Nuclear Dynamics in Heavy-Ion Reactions and the Symmetry Energy (IWND2009)”, Shanghai, China, August 23-25, 2009, to be published.
37. Zhi-Gang Xiao, Proceedings of the “International Workshop on Nuclear Dynamics in Heavy-Ion Reactions and the Symmetry Energy (IWND2009)”, Shanghai, China, August 23-25, 2009, to be published.
38. Zhao-Qing Feng, arXiv:0904.2990 [nucl-th]; Proceedings of the “International Workshop on Nuclear Dynamics in Heavy-Ion Reactions and the Symmetry Energy (IWND2009)”, Shanghai, China, August 23-25, 2009, to be published.
39. Che-Ming Ko, arXiv:0906.1602 [nucl-th]; Proceedings of the “International Workshop on Nuclear Dynamics in Heavy-Ion Reactions and the Symmetry Energy (IWND2009)”, Shanghai, China, August 23-25, 2009, to be published.
40. R. Machleidt, *Phys. Rev. C* **63** (2001) 024001.
41. V.G.J. Stoks *et al.*, *Phys. Rev. C* **49** (1994) 2950.
42. R.B. Wiringa *et al.*, *Phys. Rev. C* **51** (1995) 38.
43. R.H. Thompson, *Phys. Rev. D* **1** (1970) 110.
44. E.E. Salpeter and H.A. Bethe, *Phys. Rev.* **84** (1951) 1232.
45. G.E. Brown, in “*Mesons in Nuclei*”, M. Rho and D.H. Wilkinson eds., Vol. I, p.330, North-Holland, Amsterdam (1979).
46. G.E. Brown *et al.*, *Comments Nucl. Part. Phys.* **17** (1987) 39.
47. J. Fujita and H. Miyazawa, *Prog. Theor. Phys.* **17** (1957) 360.
48. R.G. Ellis, S.A. Coon, and B.H.J. McKellar, *Nucl. Phys.* **A438** (1985) 631.
49. Z.H. Li *et al.*, *Phys. Rev. C* **77** (2008) 034316.
50. W.H. Dickhoff, A. Faessler, and H. Mütter, *Nucl. Phys.* **A389** (1982) 492.

51. T. Klähn *et al.*, *Phys. Rev. C* **74** (2006) 035802.
52. S. Typel and H.H. Wolter, *Nucl. Phys.* **A656** (1999) 331.
53. S. Typel, *Phys. Rev. C* **71** (2005) 064301.
54. T. Gaitanos, M. Di Toro, S. Typel, V. Baran, C. Fuchs, V. Greco, and H.H. Wolter, *Nucl. Phys.* **A732** (2004) 24.
55. B. Liu, V. Greco, V. Baran, M. Colonna, and M. Di Toro, *Phys. Rev. C* **65** (2002) 045201.
56. P. Danielewicz, R. Lacey, and W.G. Lynch, *Science* **298** (2002) 1592.
57. B.A. Li and L.W. Chen, *Phys. Rev. C* **72** (2005) 064611.
58. J. Piekarewicz, arXiv:nucl-th/0607039, and references therein.
59. F. Sammarruca and P. Liu, arXiv:0806.1936 [nucl-th].
60. L.W. Chen *et al.*, arXiv:0711.1714 [nucl-th].
61. Pawel Danielewicz and Jenny Lee, arXiv:0708.2830 [nucl-th].
62. Lie-Wen Chen, Che Ming Ko, and Bao-An Li, arXiv:nucl-th/0509009.
63. Z.H. Li and H.-J. Schulze, *Phys. Rev. C* **78** (2008) 028801.
64. R.B. Wiringa, V.G.J. Stocks, and R. Schiavilla, *Phys. Rev. C* **51** (1995) 38.
65. V.G.J. Stocks, R.A.M. Klomp, C.P.F. Terheggen, and J.J. de Swart, *Phys. Rev. C* **49** (1994) 2950.
66. S.C. Pieper, V.R. Pandharipande, R.B. Wiringa, and J. Carlson, *Phys. Rev. C* **64** (2001) 014001.
67. B.K. Harrison and J.A. Wheeler in *Gravitation Theory and Gravitational Collapse* (B.K. Harrison, K.S. Thorne, M. Wakano, and J.A. Wheeler, eds.), pp. 1-177, University of Chicago Press, Chicago (1965).
68. J.W. Negele and D. Vautherin, *Nucl. Phys.* **A178** (1973) 123.
69. V.V. Psonis, Ch.C. Moustakidis, and S.E. Massen, *Modern Physics Letters A* **22** (2007) 1233.
70. C.J. Horowitz, S.J. Pollock, P.A. Souder, and R. Michaels, *Phys. Rev. C* **63** (2001) 025501.
71. Bao-An Li, Champak B. Das, Subal Das Gupta, and Charles Gale, *Phys. Rev. C* **69** (2004) 011603.
72. Ch.C. Moustakidis, *Phys. Rev. C* **76** (2007) 025805.
73. Ch.C. Moustakidis, *Phys. Rev. C* **78** (2008) 054323.
74. A.M. Lane, *Nucl. Phys* **35** (1962) 676.
75. C. Gale, G. Bertsch, and S. Das Gupta, *Phys. Rev. C* **35** (1987) 1666.
76. G.M. Welke, M. Prakash, T.T.S. Kuo, S. Das Gupta, and C. Gale, *Phys. Rev. C* **38** (1988) 2101.
77. C. Gale, G.M. Welke, M. Prakash, S.J. Lee, and S. Das Gupta, *Phys. Rev. C* **41** (1990) 1545.
78. Q. Pan and P. Danielewicz, *Phys. Rev. Lett.* **70** (1993) 2062.
79. J. Zhang, S. Das Gupta, and C. Gale, *Phys. Rev. C* **50** (1994) 1617.
80. V. Greco, A. Guarnera, M. Colonna, and M. Di Toro, *Phys. Rev. C* **59** (1999) 810.
81. P. Danielewicz, *Nucl. Phys.* **A673** (2000) 375.
82. D. Persram and C. Gale, *Phys. Rev. C* **65** (2002) 064611.
83. B.A. Li, *Phys. Rev. C* **69** (2004) 064602.
84. I. Bombaci, in *Isospin Physics in Heavy-Ion Collisions at Intermediate Energies*, Eds. B.A. Li and W. Udo Schröder (Nova Science Publishers, Inc., New York, 2001).
85. J. Rizzo *et al.*, *Nucl. Phys* **A732** (2004) 202.
86. I. Bombaci and U. Lombardo, *Phys. Rev. C* **44** (1991) 1892.
87. H.F. Zhang, Z.H. Li, U. Lombardo, P.Y. Luo, F. Sammarruca, and W. Zuo, *Phys. Rev. C* **76** (2007) 054001.

88. F. Sammarruca, *Phys. Rev. C* **77** (2008) 047301, and references therein.
89. R. Crespo and R.C. Johnson, *Phys. Rev. C* **60** (1999) 034007.
90. Benjamin J. Owen, arXiv:0903.2603 [astro-ph.SR].
91. Armen Sedrakian, *Prog. Part. Nucl. Phys.* **58** (2007) 168.
92. T. Klähn *et al.*, arXiv:0911.0654 [nucl-th].
93. A.R. Bodmer, *Phys. Rev. D* **4** (1971) 1601.
94. E. Witten, *Phys. Rev. D* **30** (1984) 272.
95. H. Terazawa, *J. Phys. Soc. Japan* **58** (1989) 3555; **59** (1990) 1199.
96. F. Weber in “*Pulsars as Astrophysical Laboratories for Nuclear and Particle Physics*”, Institute of Physics Publishing, Bristol and Philadelphia, 1999.
97. James M. Lattimer, Madappa Prakash, *Phys. Rep.* **442** (2007) 109.
98. R.C. Tolman, *Phys. Rev.* **55** (1939) 364.
99. D.J. Champion *et al.*, *Science* **230** (2008) 1390.
100. P.C.C. Freire *et al.*, arXiv:0902.2891, [astro-ph.HE].
101. M. Bejger and P. Haensel, *Astron. Astrophys.* **405** (2003) 747.
102. A.J. Faulkner *et al.*, *Astrophys. J. Lett.* **618** (2004) L119.
103. N.K. Glendenning in “*Compact Stars, Nuclear Physics, Particle Physics, and General Relativity*”, Springer-Verlag, New York, 1997.
104. A.W. Steiner, M. Prakash, J.M. Lattimer, and P.J. Ellis, arXiv:nucl-th/0410066.
105. D.J. Nice *et al.*, *Astrophys. J.* **634** (2005) 1242.
106. D.J. Nice, talk presented at the Conference “40 Years of Pulsars”, McGill University, Montreal, Canada, August 12-17 2007.
107. J.W.T. Hessels *et al.*, *Science* **311** (2006) 1901.
108. P. Kaaret *et al.*, arXiv:0611716 [astro-ph].
109. M. Baldo, G.F. Burgio, and H.-J. Schulze, *Phys. Rev. C* **58** (1998) 3688.
110. H.-J. Schulze, A. Polls, A. Ramos, and I. Vidaña, *Phys. Rev. C* **73** (2006) 058801.
111. I. Vidaña, A. Polls, A. Ramos, and H.-J. Schulze, *Phys. Rev. C* **64** (2001) 044301.
112. Dean Alderson, *Phys. Rev. C* **76** (2007) 047301.
113. Dean Alderson, *Phys. Rev. C* **77** (2007) 034304.
114. C. Samanta, P. Roy Chowdhury, and D.N. Basu, *J. Phys. G* **32** (2006) 363.
115. H.-J. Schulze, M. Baldo, and U. Lombardo, *Phys. Rev. C* **57** (1998) 704.
116. D.J. Millener, C.B. Dover, A. Gal, *Phys. Rev. C* **38** (1988) 2700.
117. P.K. Saha *et al.*, *Phys. Rev. C* **70** (2004) 044613.
118. V.R. Pandaharipande, *Nucl. Phys.* **A178** (1971) 123.
119. H.A. Bethe and M.B. Johnson, *Nucl. Phys.* **230** (1974) 1.
120. N.K. Glendenning, *Astrophys. J.* **293** (1985) 470.
121. F. Weber and M. Weigel, *Nucl. Phys.* **A493** (1989) 363c.
122. N.K. Glendenning, F. Weber, and S.A. Moszkowski, *Phys. Rev. C* **45** (1992) 844.
123. N.K. Glendenning and S.A. Moszkowski, *Phys. Rev. Lett.* **67** (1991) 2414.
124. B. Holzenkamp, K. Holinde, and J. Speth, *Nucl. Phys.* **A500** (1989) 485.
125. P. Maessen, Th. Rijken, and J. de Swart, *Phys. Rev. C* **40** (1989) 2226.
126. Th.A. Rijken, V.G.J. Stocks, and Y. Yamamoto, *Phys. Rev. C* **59** (1999) 21.
127. V.G.J. Stocks and Th.A. Rijken, *Phys. Rev. C* **59** (1999) 3009.
128. B.F. Gibson, I.R. Afnan, J.A. Carlson, and D.R. Lehman, *Prog. Theor. Phys. Suppl.* **117** (1994) 339.
129. I. Vidaña *et al.*, *Phys. Rev. C* **61** (2000) 025802.
130. I. Vidaña *et al.*, *Phys. Rev. C* **62** (2000) 035801.
131. Isaac Vidaña and Laura Tolos, *Phys. Rev. C* **62** (2000) 035801.
132. A. Rios, A. Polls, A. Ramos, and I. Vidaña, *Phys. Rev. C* **72** (2005) 024316.
133. M. Baldo, G.F. Burgio, and H.-J. Schulze, *Phys. Rev. C* **61** (2000) 055801.

- 134. M. Lacombe *et al.*, *Phys. Rev. C* **21** (1980) 861.
- 135. S. Pal *et al.*, *Phys. Rev. C* **60** (1999) 015802.
- 136. K. Schertler *et al.*, *Phys. Rev. C* **60** (1999) 025801.
- 137. F. Sammarruca, nucl-th/0801.0879.
- 138. J. Haidenbauer and Ulf-G. Meissner, *Phys. Rev. C* **72** (2005) 044005.
- 139. A. Reuber, K. Holinde, and J. Speth, *Nucl. Phys.* **A570** (1994) 543.
- 140. J. Schaffner-Bielich and A. Gal, *Phys. Rev. C* **62** (2000) 034311.
- 141. F. Sammarruca, *Phys. Rev. C* **79** (2009) 034301.
- 142. Henk Polinder, talk given at “The 20th European Conference on Few-Body Problems in Physics”, September 10-14, 2007, Pisa, Italy.
- 143. H. Dapo, B.-J. Schaefer, and J. Wambach, nucl-th/0802.2646.